Advances in Water Resources 74 (2014) 127–147

Contents lists available at ScienceDirect

Advances in Water Resources

journal homepage: www.elsevier.com/locate/advwatres

An efficient numerical model for multicomponent compressible flow in fractured porous media

Ali Zidane [a], Abbas Firoozabadi [a,b,*]

[a] Reservoir Engineering Research Institute, Palo Alto, CA, USA
[b] Yale University, New Haven, USA

ARTICLE INFO

Article history:
Received 5 March 2014
Received in revised form 12 August 2014
Accepted 18 August 2014
Available online 26 August 2014

Keywords:
Compressible flow
Fractured media
Mixed finite element
Discontinuous Galerkin
Cross flow equilibrium
IMPEC method

ABSTRACT

An efficient and accurate numerical model for multicomponent compressible single-phase flow in fractured media is presented. The discrete-fracture approach is used to model the fractures where the fracture entities are described explicitly in the computational domain. We use the concept of cross flow equilibrium in the fractures. This will allow large matrix elements in the neighborhood of the fractures and considerable speed up of the algorithm. We use an implicit finite volume (FV) scheme to solve the species mass balance equation in the fractures. This step avoids the use of Courant–Freidricks–Levy (CFL) condition and contributes to significant speed up of the code. The hybrid mixed finite element method (MFE) is used to solve for the velocity in both the matrix and the fractures coupled with the discontinuous Galerkin (DG) method to solve the species transport equations in the matrix. Four numerical examples are presented to demonstrate the robustness and efficiency of the proposed model. We show that the combination of the fracture cross-flow equilibrium and the implicit composition calculation in the fractures increase the computational speed 20–130 times in 2D. In 3D, one may expect even a higher computational efficiency.

1. Introduction

Modeling of compositional flow in subsurface fractured media is of interest in geochemical and petroleum reservoir engineering (e.g. gas injection, radioactive waste management). In reservoir simulation, different approximations are used to model flow and transport in the fracture network. Various authors have proposed a large number of models. These models are mainly categorized into two classes: the dual-continuum model and the discrete-fracture/discrete matrix model (DFDM). The most accurate and physically realistic model is the DFDM approach where the fractures and the matrix are both described explicitly in the computational domain [1–9]. In order to capture the matrix/fracture discontinuities in concentration and/or saturation Nick and Matthäi [10] proposed a method in which the mesh at the fracture/matrix interface is split by adding extra nodes/degree of freedom and solve the equations accordingly. This model requires fine grids which makes implementation in field scale fracture network expensive.

The dual-continuum models are widely used to simulate flow in fractured media [11–17] because of low computational cost. The dual-porosity model was first introduced in 1960 [11] and was later in 1963 advanced further [12] to simulate single-phase flow in fractured media. The model was then extended to multiphase flow [13,14,18]. The flow domain is constituted by the connected fracture network, and the matrix domain is constituted by the low permeability rock that provides the storage. In the dual-porosity models, a transfer function that may vary spatially in the domain is used to describe the exchange between the fracture network and the rock matrix. An extension of the dual-porosity model was made by Haggerty and Gorelick [19] employing a so-called multirate mass transfer model at different transfer rates based on the properties of permeable media. Di Donato et al. [20] applied the multiple transfer functions in a single simulation grid block and recently, Geiger et al. [21] extended this model to two-phase incompressible flow. A hybrid model called a fracture-only model was proposed by Unsal et al. [22] for incompressible flow using a dual-porosity approach. A transfer function is used to account for the fracture/matrix exchange, and the fractures are modeled using the discrete-fracture approach. The fracture-only model is based on the assumption that all the fractures are interconnected.

The mass transfer between the fractures and the matrix is described by empirical functions that incorporate some ad-hoc shape factors in all the dual-porosity models. The appropriate shape factors are not well established for compositional and compressible flow. In principle, it is possible to compute these transfer

* Corresponding author at: Reservoir Engineering Research Institute, Palo Alto, CA, USA.

http://dx.doi.org/10.1016/j.advwatres.2014.08.010
0309-1708/

functions to describe fracture-matrix exchange (see e.g. [23]) but as mentioned in [1], there is no theory to calculate the shape factors which determine the exchange between the two domains in two-phase flow with capillary and gravity effects as well as in compositional compressible conditions. In case of diffusion flux, the transfer function approach becomes even less accurate [24].

The control-volume finite element (CVFE) has been used to solve two-phase flow equations in fractured media combined with the Galerkin finite element (GFE) method [25–27]. The fracture entities are embedded within the matrix control-volume in the CVFE method. The calculation of the matrix–fracture flux is therefore avoided and practically there is no difficulty in computing the fracture–fracture flux. However this approach has not been fully examined for compositional modeling and for two-phase flow including gravity and/or capillary pressure effect.

A simplification of the single-porosity model in the discrete fracture approach as proposed in [28,29] assumes that the fracture aperture is small compared to the matrix scale. The fractures are represented by $(n-1)$-dimensional elements in an n-dimensional domain. Hoteit and Firrozabadi [30] used the cross-flow equilibrium (CFE) concept in the discrete fracture approach to model multicomponent compressible flow in fractured porous media. The CFE approach assumes that the pressure in a fracture element is equal to the pressure in the surrounding matrix elements (Fig. 1a and b). This simplification is much more efficient than the single-porosity model and overcomes the limitations of the dual-porosity models. On the other hand, the CFE assumption requires that the matrix grids next to fractures to be small so that the assumption of equality of pressure and composition in the neighborhood matrix elements and fractures is accurate. The size of the time step in the explicit scheme is restricted by the Courant–Freidricks–Levy (CFL) condition. The CFL condition forces the time step to be less than the necessary time for flow to pass through one grid block. The small elements near the fractures impose a severe CFL condition on the time step in the explicit composition calculations. Hoteit and Firoozabadi [31] found that for a fractured reservoir of few kilometers length, the matrix grid-cell size next to the fractures should be in the order of tens of centimeters. A new approach was introduced by Hoteit and Firoozabadi [1] to overcome the limitations of the CFE model and was applied for incompressible two-phase flow in fractured media. In this approach there is a significant increase in computational speed. The essence of the idea by Hoteit and Firoozabadi [1] relates to the constant pressure across the fracture width which is the same as the cross-flow equilibrium across the fracture elements. Note that the cross-flow equilibrium does not imply that convective velocity is zero along the fractures.

In this work we propose a model based on the ideas for incompressible flow suggested by Hoteit and Firoozabadi [1]. There are, however, important differences due to fluid compressibility which requires a pressure equation as we will discuss later. The pressure is assumed to be equal along the fracture width. We refer to the model as the fracture cross flow equilibrium (FCFE). The mass transfer of the species between the fracture and the matrix and inside the fracture network is provided by the hybridized mixed finite element method (MFE). The MFE is more accurate than the traditional finite element (FE) and control volume finite element (CVFE) methods in flux calculation [32,33]. It also has low grid orientation [34]. In addition to the grid-cell pressures, the MFE provides the pressures at the grid-cell interfaces which are used to accurately approximate the velocity field even in highly heterogeneous fractured media [1,30,35–37]. Because of its powerful feature, the MFE is used in this work to discretize Darcy's equation for compressible flow. The species mass balance equation in the matrix is discretized by the discontinuous Galerkin (DG) method [38,39]. The DG method is mass conservative at the element level and has low numerical dispersion. The use of the high-order numerical scheme may produce nonphysical oscillations. To overcome these oscillations, a multidimensional slope limiter is used to

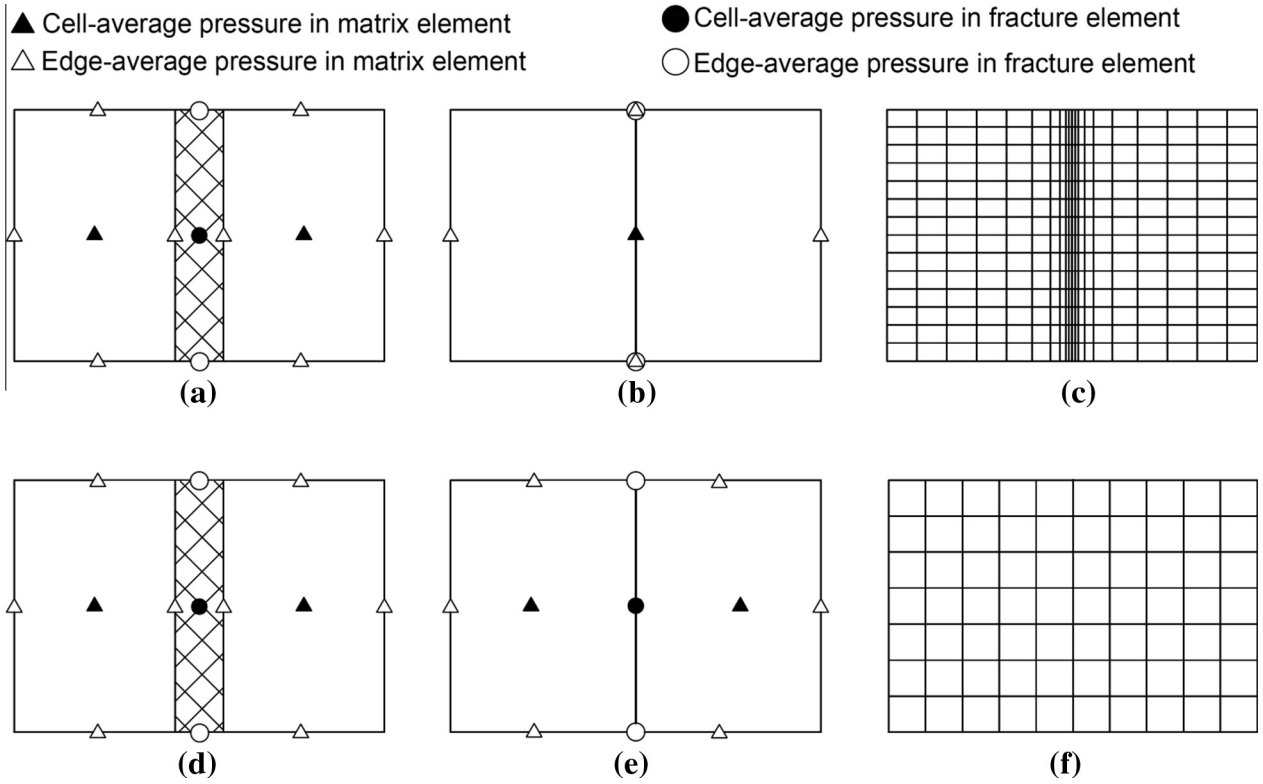

Fig. 1. Physical (a,d) and computational (b,c,e,f) representations in the CFE (a,b,c) and FCFE (d,e,f) approach.

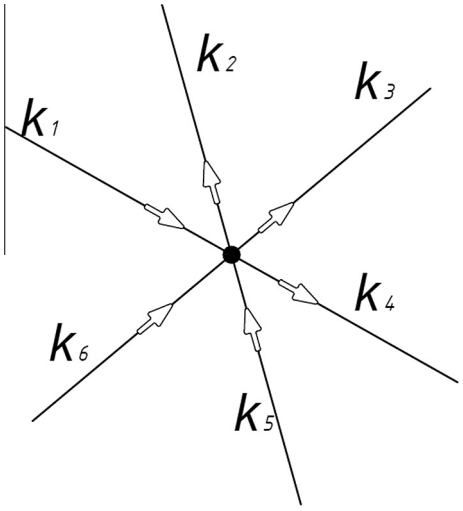

Fig. 2. Multiple intersecting fractures.

Table 1
Relevant properties of porous media and initial conditions (C_1 and C_3 are in mole fraction). Example 1.

Injection gas [–]	0.8 C_1	0.2 C_2
Initial fluid [–]	0.0 C_1/C_2	1.0 C_3
Pressure [bar]	50	
Temperature [K]	397	
Porosity [–]	0.2	
Permeability [md]	1	
Injection rate [PV/year]	0.1	

reconstruct the concentration distribution over the simulation domain [40,41]. The slope limiter imposes local constraints in a geometric manner in such a way that the reconstructed solution satisfies an appropriate maximum principle. With these constraints, the value of the variable (molar concentration in our study) at any node should always remain between the minimum and the maximum values of the cell averages of all elements containing the node. Efficiency and robustness of the combined MFE and DG model has been demonstrated in numerous publications [see e.g. 42,43].

The species mass balance equation is linked to the pressure equation by an implicit-pressure-explicit concentration (IMPEC) approach. The IMPEC approach is more efficient than the fully-implicit method [44]. The explicit method in the fractures imposes a strong limitation on the time step due to the stringent CFL stability constraint for the small elements in the fracture network. To overcome the severe CFL constraint in the fracture network, we use an implicit scheme in the fracture network where a finite volume (FV) approach is used to discretize the species mass balance equation.

The rest of the manuscript is organized as follows: in the next section we provide a description of the proposed model, followed by the differential equations describing the multicomponent compressible flow in fractured porous media. Then we present the discretization of the pressure and the species mass balance equations in the rock matrix and in the fracture network. We present four numerical examples to demonstrate the efficiency and accuracy of the proposed algorithm. In addition to these examples we have performed computations for a higher viscosity fluid saturating the domain and a lower injection fluid viscosity. The results for this fluid combination are similar to other fluids to be presented later.

2. Proposed model

Modeling of immiscible fluid flow in fractured porous media has been studied extensively in the literature [45–47]. However, the work on compositional compressible flow in fractured media is limited. The CFE approach has been developed to accurately model compositional, multicomponent, compressible flow in fractured porous media. Hoteit and Firoozabadi [30] proposed a model for compressible single-phase flow in fractured porous media based on the CFE approach. In their work [30] the pressures are updated iteratively and the species equations are solved explicitly. The work in [30] has been extended from two-phase flow to three-phase compositional flow in fractured media [48–51]. In the CFE approach pressure at the fracture elements is set to be equal to pressure at the adjacent matrix elements (Fig. 1a and b). This approach is accurate when the matrix elements near the fractures are small (Fig. 1c). When an IMPEC scheme is used the CFL constraint makes the simulation expensive. In this work we do not use the CFE approach between the fracture and the adjacent matrix grid cells. We assume a constant pressure across the fracture width (Fig. 1d and e). The pressures and concentrations in the fracture and in the adjacent matrix grid cells may not be the same. The proposed model provides accurate calculation of the species concentration; it alleviates the need for small elements in the matrix grid cells near the fractures which reduces significantly the CFL condition (Fig. 1f). To avoid the CFL constraint in the small fracture elements a fully implicit scheme is used to compute the species mass balance equation in the fracture network, as will be discussed in the following sections.

3. Mathematical model

3.1. Governing equations in the matrix

The rock matrix and the discrete fractures have generally different geometrical dimensions in the simulation domain (n – D for the matrix domain and $(n-1)$ – D for the fracture network). The governing equations are, therefore, treated separately. The superscript m denotes the matrix; the superscript f denotes the fractures. The mass balance of component i in a miscible and compressible flow is given by the following system of equations [30]:

$$\begin{aligned} &\emptyset^m \frac{\partial c_i^m}{\partial t} + \nabla \cdot (c_i^m \boldsymbol{v}^{\boldsymbol{m}}) - f_i^m = 0, \quad i = 1 \ldots n_c \text{ in } \Omega \times (0,\tau) \\ &c_i = z_i c \\ &\sum_{i=1}^{n_c} z_i = 1 \end{aligned} \tag{1}$$

In the above equations, $\emptyset$ denotes the porosity, $\boldsymbol{v}$ the velocity field, c the overall molar density; c_i, z_i and f_i are the molar density, the mole fraction and the sink/source term of component i in the mixture, respectively. Ω is the 2-D computational domain and τ denotes the simulation time and n_c is the number of components. We neglect diffusion in Eq. (1).

The flow in porous media is described by Darcy's law:

$$\boldsymbol{v} = -\frac{\boldsymbol{k}}{\mu}(\nabla p - \rho \boldsymbol{g}) \tag{2}$$

where $\boldsymbol{k}$ is the absolute permeability tensor, μ the dynamic viscosity, p the pressure, ρ the mass density and $\boldsymbol{g}$ the gravitational acceleration. In this work the effect of gravity is not considered. In a forthcoming work we will extend the model to compositional two-phase flow with gravity effect.

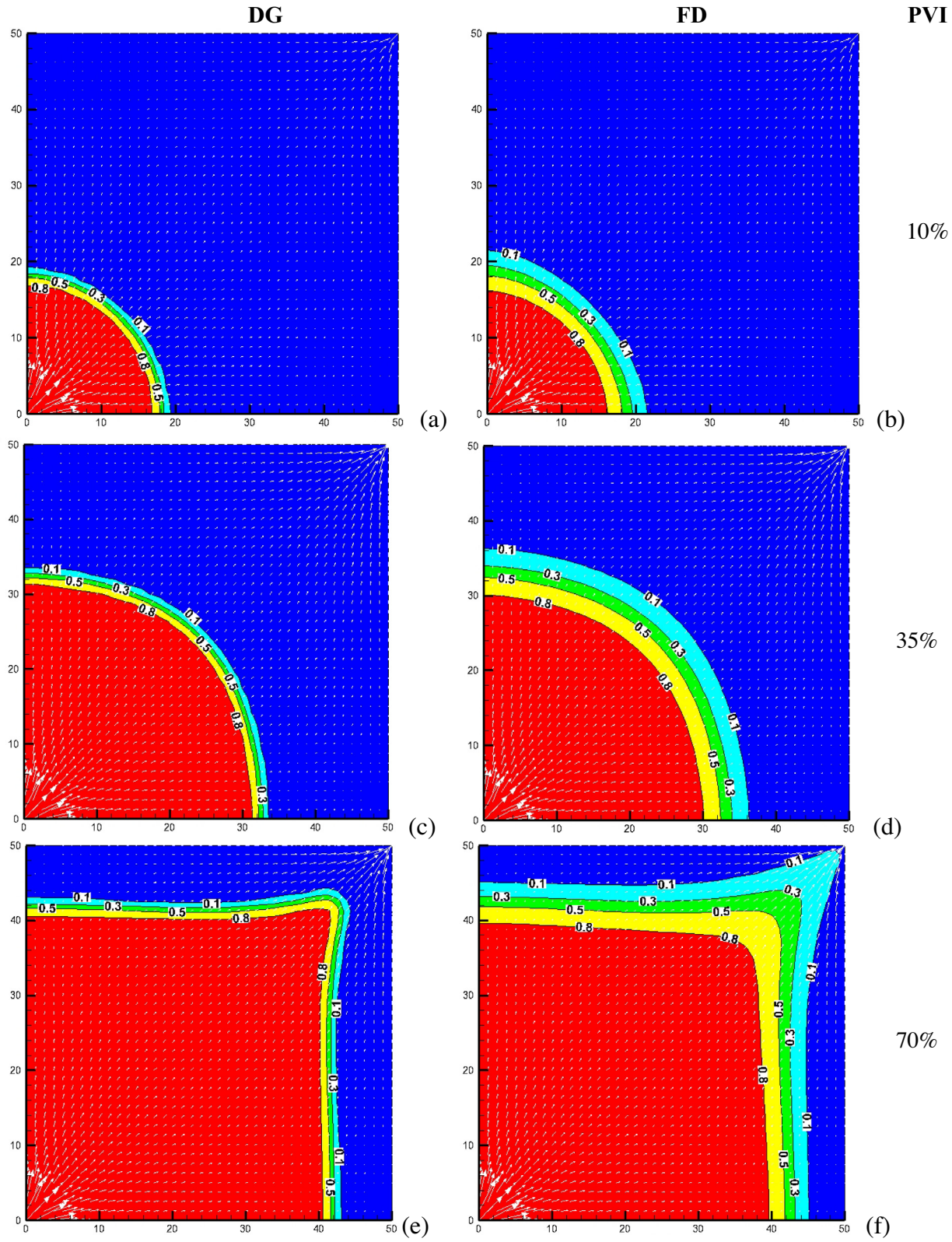

Fig. 3. Methane composition (mole fraction) profile at different PVI from the MFE-DG and the MFE-FD methods in 40 × 40 mesh; white arrows represent the velocity field. Example 1 (distances in meters).

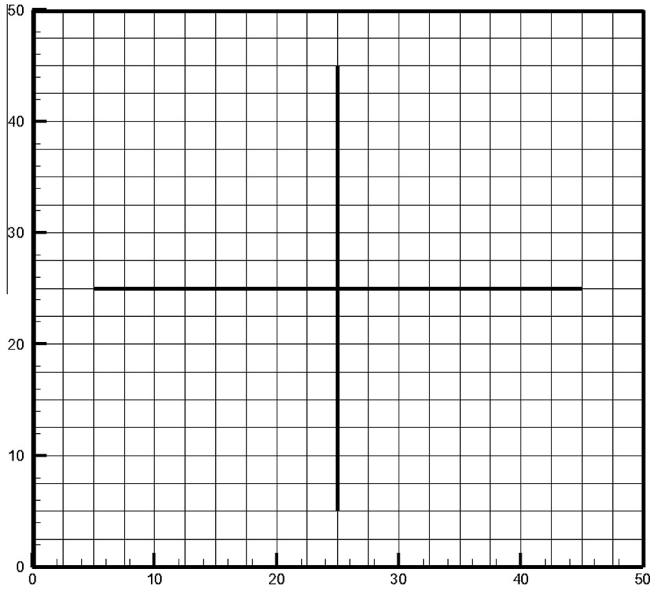

Fig. 4. Domain size of 50 × 50 m^2 showing the 20 × 20 coarse mesh used with two intersecting fractures. Example 2.

Table 2
Relevant properties of porous media and initial conditions (C_1 and C_3 are in mole fraction). Example 2.

Injection gas	0.8 C_1	0.2 C_2
Initial fluid	0.0 C_1/C_2	1.0 C_3
Pressure [bar]	50	
Temperature [K]	397	
Porosity [–]	0.2	
Matrix permeability [md]	1	
Fracture permeability [md]	1.d6	
Fracture thickness [mm]	2	
Injection rate [PV/year]	0.1	

The Peng–Robinson equation of state (EOS) [52] is used to describe the molar density c as a function of the composition, temperature and pressure as follows:

$$\begin{aligned} c &= \frac{p}{ZRT} \\ Z^3 - (1-B)Z^2 + (A - 3B^2 - 2B)Z - (AB - B^2 - B^3) &= 0 \\ \rho &= \sum_{i=1}^{n_c} M_i c_i \end{aligned} \tag{3}$$

Z is the compressibility factor, R the gas constant, T the temperature, and M_i the molar mass of component i. The expressions for the constants A and B could be found in [53]. To complete the system of equations, we use the volume balance from [54,55] to compute the pressure field for the compositional compressible flow. Note that in incompressible flow there is no need for volume balance. The expression for volume balance is given by [54,55]:

$$\emptyset^m C_t^m \frac{\partial p^m}{\partial t} + \sum_{i=1}^{n_c} \bar{V}_i^m (\nabla.(c_i^m \boldsymbol{v}^{\boldsymbol{m}}) - f_i^m) = 0 \tag{4}$$

where C_t is the compressibility, $\bar{V}_i$ is the partial molar volume of component i in the mixture; expressions for C_t and $\bar{V}_i$ are provided in Appendix A.

Eqs. (1) and (4) are subject to initial and boundary conditions as follows:

$$\begin{aligned} &p(\boldsymbol{x}, 0) = p^0(\boldsymbol{x}), && \text{in } \Omega \\ &p(\boldsymbol{x}, t) = p^D(\boldsymbol{x}, t), && \text{on } \Gamma^D \times (0, \tau) \\ &z_i(\boldsymbol{x}, 0) = z_i^0(\boldsymbol{x}), && i = 1 \ldots n_c \text{ in } \Omega \\ &cz_i(\boldsymbol{x}, t)\boldsymbol{v} \cdot \boldsymbol{n} = q_i^N(\boldsymbol{x}, t), && i = 1 \ldots n_c \text{ on } \Gamma^N \times (0, \tau) \end{aligned} \tag{5}$$

where p^0 and p^D are the initial pressure and the imposed pressure on the boundary Γ^D, q_i^N is the injection rate of component i across the boundary Γ^N and $\boldsymbol{n}$ and $\boldsymbol{x}$ denote the unit outward normal vector, and spatial coordinates, respectively.

3.2. Governing equations in the fractures

The mass balance equations in the fractures are integrated along the fracture width ε and in the $(n-1)-D$ are expressed by:

$$\emptyset^f \frac{\partial c_i^f}{\partial t} + \nabla \cdot (c_i^f \boldsymbol{v}^{\boldsymbol{f}}) - \bar{Q}_i^f - f_i^f = 0, \quad i = 1 \ldots n_c \tag{6}$$

In the above equation, the term $\bar{Q}_i^f$ is the volumetric flux across the matrix-fracture boundaries Q^f multiplied by the molar concentration of component i in the mixture. Similarly to the matrix domain, the pressure field in the fractures is obtained from:

$$\emptyset^f C_t^f \frac{\partial p^f}{\partial t} + \sum_{i=1}^{n_c} \bar{V}_i^f \left(\nabla.(c_i^f \boldsymbol{v}^{\boldsymbol{f}}) - c_i^f Q^f - f_i^f \right) = 0 \tag{7}$$

The calculation of the transfer flux is discussed in the following section.

4. Discretization of the pressure equation

4.1. Discretization in the matrix

In this section we show how to treat the volumetric flux that represents the exchange rate between the matrix and the fracture network when solving the pressure equation. Here, we present for the first time how to couple the pressure equation and the species transport equation in a compressible flow in fractured media without the need to calculate a transfer function and/or impose approximations at the matrix- fracture interface.

The hybridized mixed finite element (MFE) method with the lowest order Raviart–Thomas basis space is used to discretize the volumetric flow in the matrix. Discretization of Eq. (2) with the MFE yields the expression of the flux $q_{K,E}^m$ at the edge E of the matrix element K (see Appendix B for details):

$$q_{K,E}^m = \alpha_{K,E}^m P_K^m - \sum_{E' \in \partial K} \beta_{K,E,E'}^m Tp_{E'}^m \tag{8}$$

In the above equation, P_K^m represents the cell-average pressure, and $Tp_{E'}^m$ the face-average pressure in all the faces of element K. Details of constants $\alpha_{K,E}^m$ and $\beta_{K,E,E'}^m$ are provided in Appendix B.

The continuity of fluxes and pressures at all the interfaces are imposed at each interface E between two adjacent matrix elements K and K'. Three different possibilities could arise:

If the intersection between two matrix elements is a fracture (fractures are represented in $(n-1)-D$ in an $n-$D domain) then the following equalities apply:

$$\begin{cases} Tp_{K,E}^m = Tp_{K',E}^m = P_E^f \\ q_{K,E}^m + q_{K',E}^m = Q_E^f \end{cases} \tag{9}$$

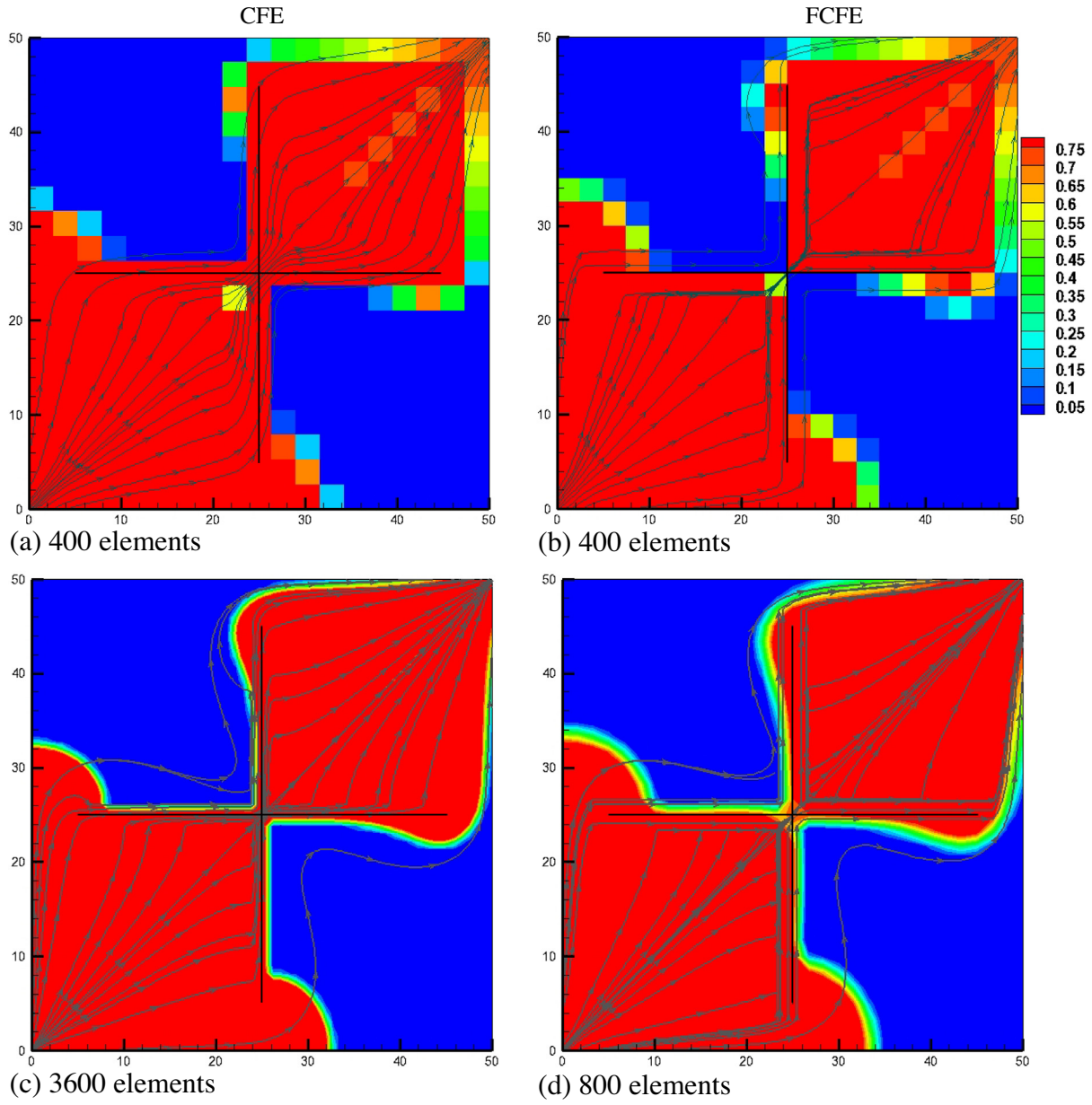

Fig. 5. Methane composition (mole fraction) profile and streamlines at 0.7 PVI, from the CFE and FCFE approaches with different mesh refinements. Example 2 (distances in meters).

where Q_E^f is the total flux across the two sides of the fracture E with the matrix elements K and K', and P_E^f is the cell average pressure of the fracture element E.

If the interface E between the two matrix elements K and K' is not a fracture and is not a boundary, then the continuity of pressure and flux implies:

$$\begin{cases} Tp_{K,E}^m = Tp_{K',E}^m \\ q_{K,E}^m + q_{K',E}^m = 0 \end{cases} \tag{10}$$

Table 3
CPU time in seconds for different mesh refinements, at 0.7 PVI. Example 2.

Number of elements	400	800	3600
CFE	4	–	251
FCFE	3	9	–

If the interface E is at the domain's boundary then:

$$\begin{cases} Tp_{K,E}^m = Tp_E^D \\ q_{K,E}^m = q_E^N \end{cases} \tag{11}$$

where Tp_E^D is a Dirichlet boundary conditions, and q_E^N is a Neumann boundary condition. In this work, however, we assume an impermeable boundary and set $q_{K,E}^m$ to be zero at the boundary.

Writing Eqs. (9)–(11) for all interfaces E of the domain and using the expression of the matrix fluxes given in Eq. (8) we construct the system of pressure equations that relates the matrix interfaces to the fracture elements:

$$\begin{bmatrix} R^{T,m,m} \\ R^{T,m,f} \end{bmatrix} [\boldsymbol{P^m}] - \begin{bmatrix} M^{m,m} & M^{m,f} \\ M^{f,m} & M^{f,f} \end{bmatrix} \begin{bmatrix} \boldsymbol{Tp^m} \\ \boldsymbol{P^f} \end{bmatrix} = \begin{bmatrix} 0 \\ \boldsymbol{Q^f} \end{bmatrix} \tag{12}$$

where $\boldsymbol{P^m}$ contains the matrix cell-average pressures, $\boldsymbol{Tp^m}$ contains the matrix edge-average pressures and $\boldsymbol{P^f}$ contains the fracture cell-

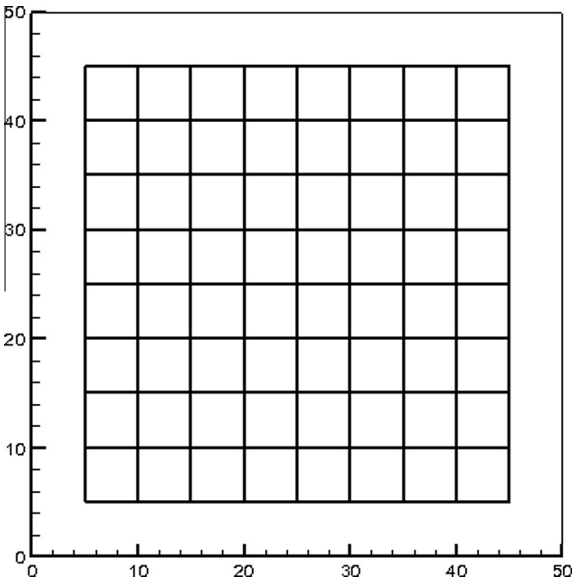

Fig. 6. Domain of the fracture network, mesh not shown. Example 3 (distances in meters).

average pressures. At the right side, $\boldsymbol{Q^f}$ denotes the volumetric flux exchange between the matrix and all the fracture elements. Treatment of this term will be discussed later. The matrices of Eq. (12) are defined in Appendix B.

Integrating Eq. (4) by parts, we get the discretized form of the pressure equation in a matrix element K by:

$$\emptyset^m C_t^m \frac{P_K^{n+1,m} - P_K^{n,m}}{\Delta t} + \sum_{i=1}^{n_c} \bar{V}_i^m \int_{\partial K} c_i^m \boldsymbol{v^m} \boldsymbol{n}_{\partial K} - \sum_{i=1}^{n_c} \bar{V}_i^m \int_K f_i^m = 0 \qquad (13)$$

Using the expression of the flux $q_{K,E}^m$ given in Eq. (8) and replacing it in Eq. (13):

$$\left(\frac{\emptyset^m C_t^m |K|}{\Delta t} + \bar{\alpha}_K^m\right) P_K^{n+1,m} - \sum_E \bar{\beta}_{K,E}^m Tp_{K,E}^{n+1,m} = F_{i,K}^m \qquad (14)$$

The expressions for $\bar{\alpha}_K^m$, and $\bar{\beta}_{K,E}^m$ are obtained by multiplying α_K^m and $\beta_{K,E}^m$ by the partial molar volumes. The matrix form of Eq. (14) is given by:

$$[\bar{D}^m][\boldsymbol{P^m}] - [\bar{R}^{m,m} \quad \bar{R}^{m,f}] \begin{bmatrix} \boldsymbol{Tp^m} \\ \boldsymbol{P^f} \end{bmatrix} = [F^m] \qquad (15)$$

The matrices $\bar{D}^m$, $\bar{R}^{m,m}$ and $\bar{R}^{m,f}$ are readily derived from Eq. (14) using the first expression in Eq. (9).

4.2. Discretization in the fractures

The discretization in the fractures is similar to the discretization in the matrix domain. The difference is that the fractures are represented by $(n-1)-$D in an $n-$D domain, hence the fracture intersections are represented by single points in the 2-D domain. Another difference is that the volumetric transfer flux appears in the pressure equation in the fracture network. The volumetric transfer flux across the fracture interface e in the MFE formulation in a fracture element k is given by:

$$q_{k,e}^f = \alpha_{k,e}^f P_k^f - \sum_{e' \in \partial k} \beta_{k,e,e'}^f Tp_{e'}^f \qquad (16)$$

The low dimensional order of the fracture representation allows two fractures to have the same intersection (see Fig. 2). The intersection of multiple fractures in 2D is represented by a single point; hence, it has no volume. The parameters $\alpha_{k,e}^f$ and $\beta_{k,e,e'}^f$ are similar to those defined in Eq. (8). The zero accumulation at the multiple fracture intersection and the continuity of the pressure impose:

$$\begin{cases} \sum_{i=1}^{n_t} q_{k_{i,e}}^f = 0 \\ Tp_{k_{i,e}}^f = Tp_e^f, \quad i = 1 \ldots n_t \end{cases} \qquad (17)$$

where n_t represents the number of intersecting fractures (Fig. 2). Replacing the expression for the flux in Eq. (17) and using the pressure continuity at the intersections from the second expression in Eq. (17) we obtain the system of equations in a matrix form with unknowns as the fracture cell-average pressures and the fracture-interface pressures as follows:

$$[R^{T,f}][\boldsymbol{P^f}] - [M^f][\boldsymbol{Tp^f}] = [0] \qquad (18)$$

Integrating the fracture pressure equation (Eq. (7)) for each fracture element, we derive the following system in a matrix form:

$$[\bar{D}^f][\boldsymbol{P^f}] - [\bar{R}^f][\boldsymbol{Tp^f}] = [F^f] + [\boldsymbol{Q^f}] \qquad (19)$$

The matrices $\bar{D}^f$, and $\bar{R}^f$ are similar to those in Eq. (15). $\boldsymbol{Q^f}$ is the matrix-fracture transfer flux previously defined.

4.3. Global system of equations

The coupling of the matrix and the fracture pressures is made through the continuity of the pressure at the matrix grid cell interfaces and the fracture grid cell, and through the transfer flux that appears in Eqs. (12) and (19). To avoid the calculation of the fracture-matrix fluxes, we subtract Eq. (19) from the second expression in Eq. (12) and construct the equation for the global system by combining Eqs. (12), (15), (18) and (19) to obtain:

$$\begin{bmatrix} \bar{D}^m & -\bar{R}^{m,m} & -\bar{R}^{m,f} & 0 \\ -R^{T,m,m} & M^{m,m} & M^{m,f} & 0 \\ -R^{T,m,f} & M^{m,f} & M^{f,f} + \bar{D}^f & -\bar{R}^f \\ 0 & 0 & R^{T,f} & M^f \end{bmatrix} \begin{bmatrix} \boldsymbol{P^m} \\ \boldsymbol{Tp^m} \\ \boldsymbol{P^f} \\ \boldsymbol{Tp^f} \end{bmatrix} = \begin{bmatrix} f^m \\ 0 \\ f^f \\ 0 \end{bmatrix} \qquad (20)$$

With a simple Gaussian elimination we construct the final system of equations:

$$\begin{bmatrix} A^{m,m} & A^{m,f} & 0 \\ A^{m,f} & A^{f,f} & -\bar{R}^f \\ 0 & R^{T,f} & M^f \end{bmatrix} \begin{bmatrix} \boldsymbol{Tp^m} \\ \boldsymbol{P^f} \\ \boldsymbol{Tp^f} \end{bmatrix} = \begin{bmatrix} V^m \\ V^f \\ 0 \end{bmatrix} \qquad (21)$$

In the above equation the number of unknown pressures equals the number of interfaces in the matrix domain ($\boldsymbol{Tp^m} + \boldsymbol{p^f}$) plus the number of interfaces in the fracture network ($\boldsymbol{Tp^f}$). The system in Eq. (21) is sparse and positive definite. The calculation of the matrix grid-cell average pressures is made through a simple back substitution using the first expression in Eq. (20).

Table 4
Relevant properties of porous media and initial conditions (C_1 and C_2 are in mole fraction). Example 3.

Injection gas	1.0 C_1
Initial fluid	1.0 C_2
Pressure [bar]	50
Temperature [K]	397
Porosity [–]	0.2
Matrix permeability [md]	1
Fracture permeability [md]	1.d5
Fracture thickness [mm]	2
Injection rate [PV/year]	0.1

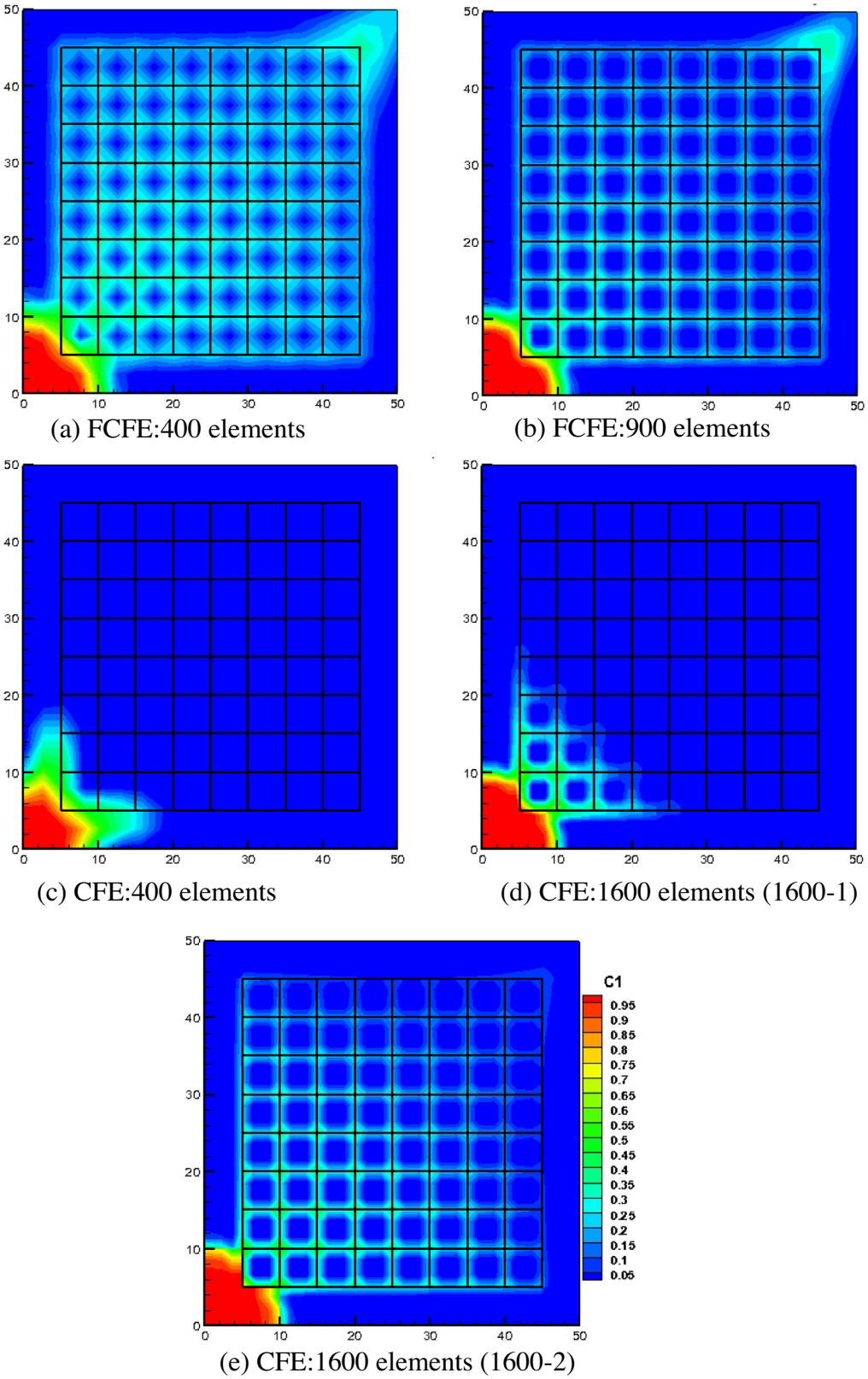

Fig. 7. Methane composition (mole fraction) profile at 0.05 PVI in different mesh refinements in the FCFE and CFE methods. Example 3 (distances in meters).

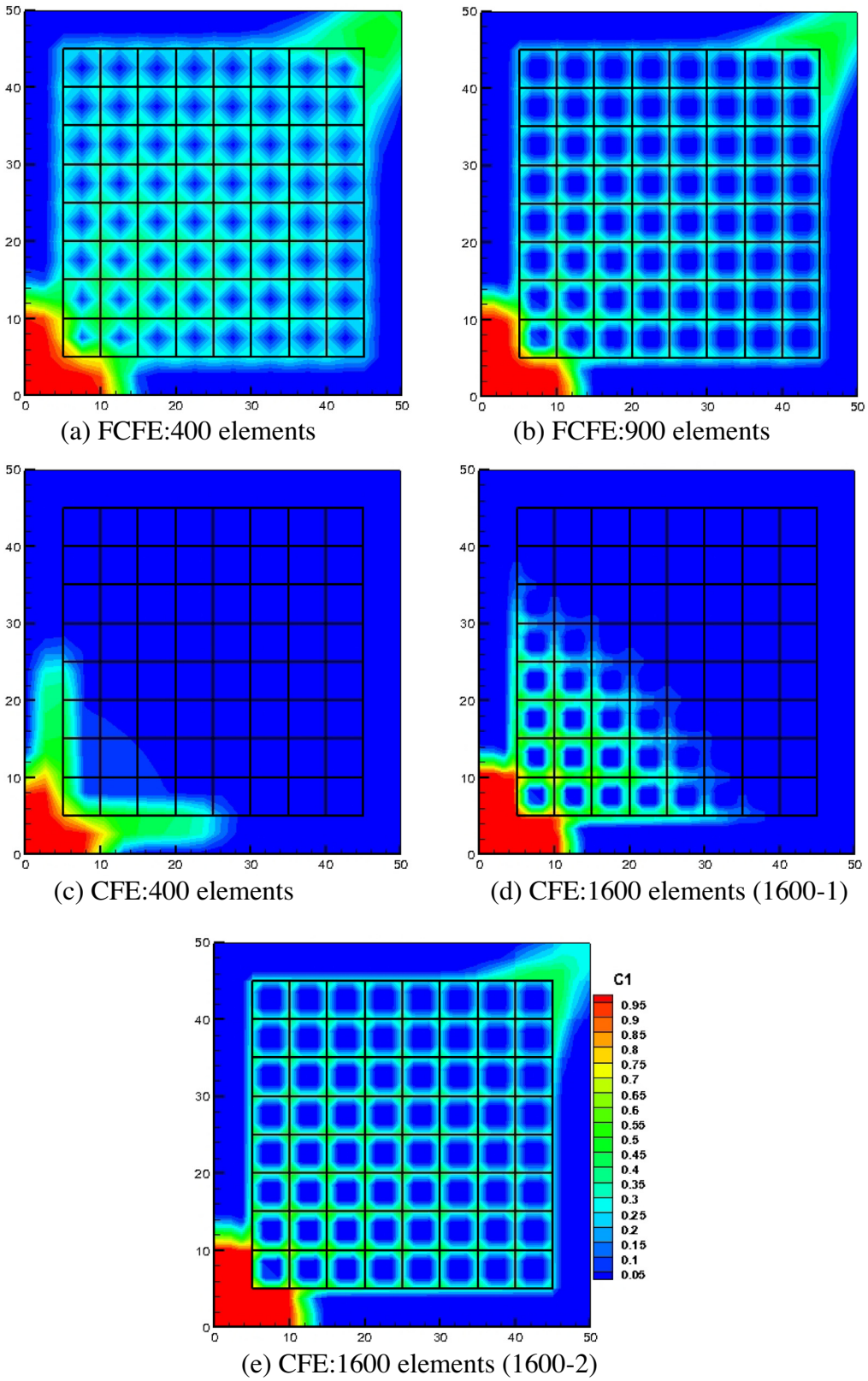

Fig. 8. Methane composition (mole fraction) profile at 0.1 PVI in different mesh refinements in the FCFE and CFE methods. Example 3 (distances in meters).

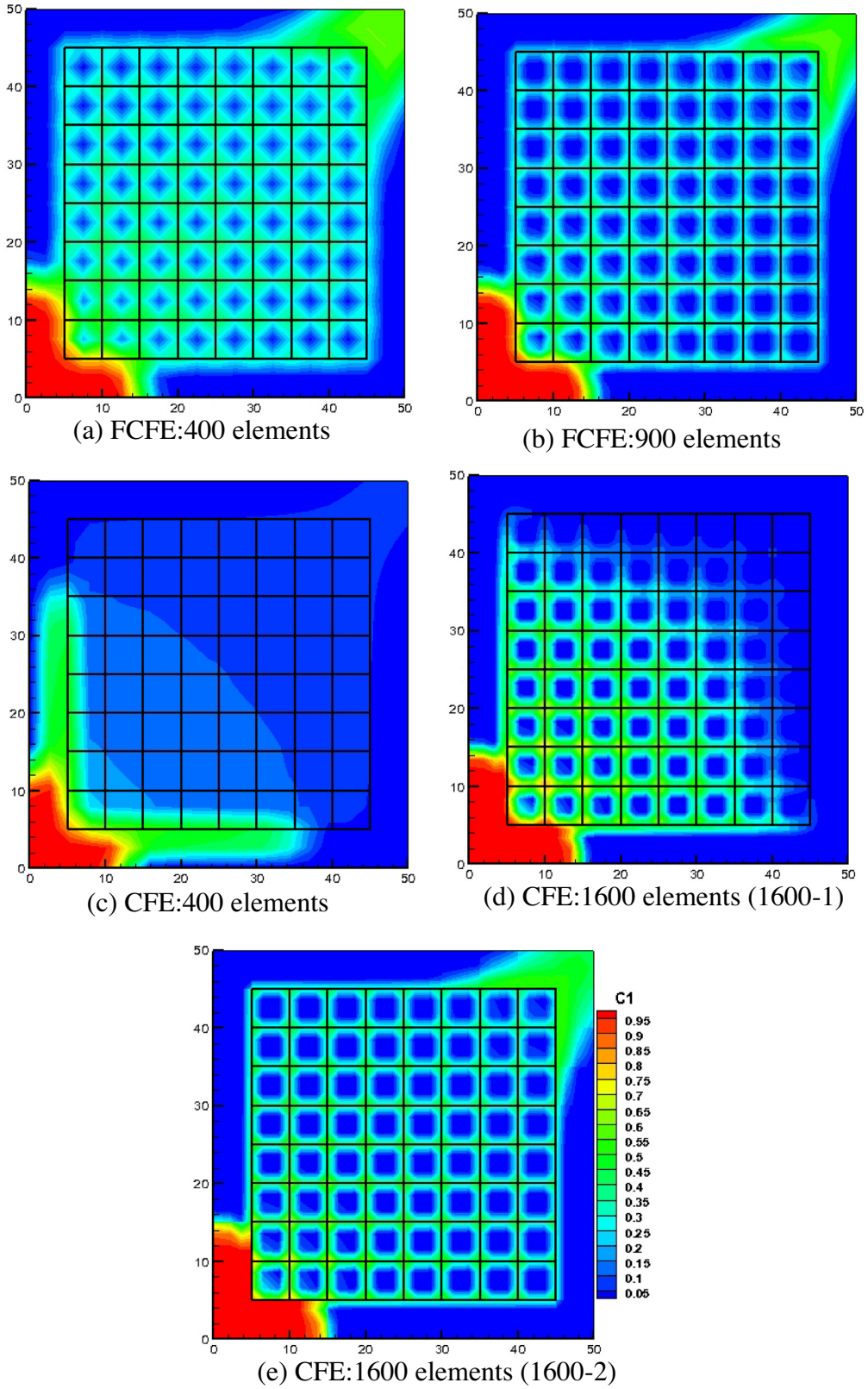

Fig. 9. Methane composition (mole fraction) profile at 0.2 PVI in different mesh refinements in the FCFE and CFE methods. Example 3 (distances in meters).

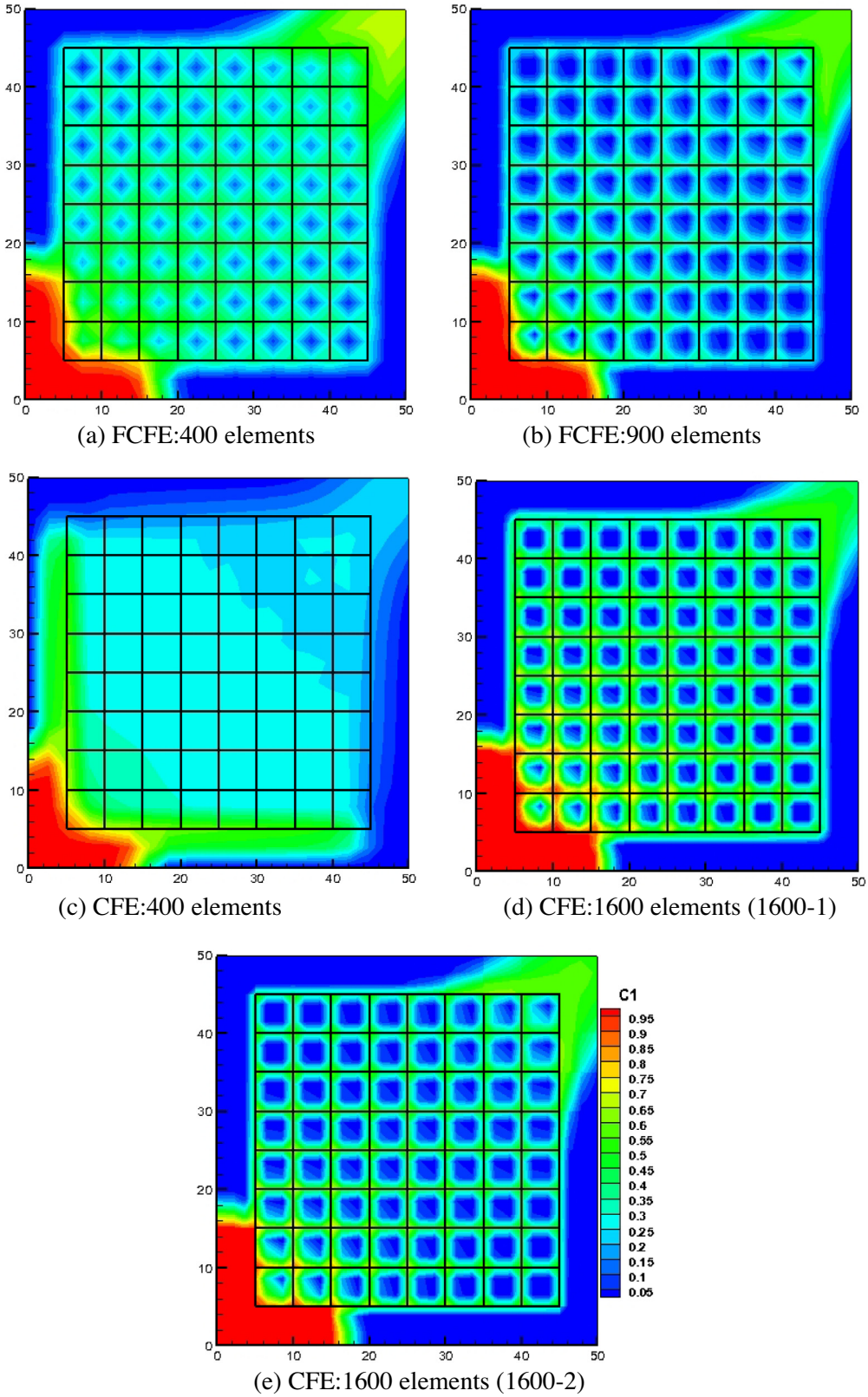

Fig. 10. Methane composition (mole fraction) profile at 0.4 PVI in different mesh refinements in the FCFE and CFE methods. Example 3 (distances in meters).

5. Discretization of the species transport equation

5.1. Discretization in the matrix

The DG method is used to discretize the species transport equation in the matrix. In the DG method, different orders of approximations could be used; in this work we use a bilinear approximation on the element level. Coupled with the MFE method, the DG provides accurate results and efficient in CPU time [26,27,31–33,43]. An explicit approach is used to approximate the transport equation in the matrix. Multiplying the first expression in Eq. (1) by the shape function $\varphi_{K,l}$ and integrating over each matrix element K we get:

$$\sum_{i=1}^{n_j}\frac{dc^m_{i,K,j}}{dt}\int_K \emptyset^m_K\varphi_{K,l}\varphi_{K,j}=\int_K\varphi_{K,l}f^m_i + \sum_{j=1}^{n_j}\sum_{E=1}^{n_E}\left(c^m_{i,K,j}\int_K\varphi_{K,j}\mathbf{w}_{K,E}\nabla\varphi_{K,l}-\frac{\bar{c}^m_{i,K,E,j}}{|E|}\int_E\varphi_{K,l}\varphi_{K,j}\right) \tag{22}$$

In the above equation $c^m_{i,K,j}$ is the molar density of component i at node j where n_j is the number of nodes in the matrix element K. $\bar{c}^m_{i,K,E,j}$ is the upstream molar density of component i at node j of interface E, where n_E is the total number of interfaces in a matrix element K. The system of ordinary differential equations of order n_j is obtained by writing Eq. (22) over each element K in the matrix domain. An explicit scheme for the species transport equation is used, coupled with a slope limiter stabilization to overcome the nonphysical oscillations.

5.2. Discretization in the fractures

The small volume of the fracture elements imposes a severe CFL condition on the time step if an explicit scheme is used. To overcome the CFL restriction and to avoid the expensive DG approximation in the fractures, a finite volume method with a first-order implicit method is applied in the fractures. The numerical dispersion in the fracture that arises from the use of an implicit scheme may not be significant since a higher-order spatial scheme (DG) is used in the matrix domain. The species transport equation in the fracture is written as:

$$\emptyset^f_k\frac{c^{f,n+1}_{i,k}-c^{f,n}_{i,k}}{t}+\sum_{e=1}^{n_e}\bar{c}^{f,n}_{i,e}q^{f,n}_{k,e}=\bar{Q}^{f,K_1}_i+\bar{Q}^{f,K_2}_i+f^{f,n}_{i,k} \tag{23}$$

In the above equation $\bar{c}^{f,n}_{i,e}$ denotes the upstream value of the molar density. We will discuss how to calculate molar density in multiple intersecting fractures in the next section. The term $\bar{Q}^{f,K_j}_i$ ($j = 1, 2$) in the above equation is equal to the volumetric flux multiplied by the molar density of component i. The two terms represent the interaction of the adjacent two matrix elements K_1 and K_2 around the fracture element k and they are treated differently in Eq. (23). When $\bar{Q}^{f,K_j}_i$ ($\bar{Q}^{f,K_1}_i$, $\bar{Q}^{f,K_2}_i$ or both) is an influx from the matrix through the fractures, then $\bar{Q}^{f,K_j}_i$ is treated explicitly. Otherwise it is treated implicitly. Eq. (23) is written for all the fracture elements and the system of equations is linearized and solved using the Newton–Raphson method. In all the calculations we have performed in the Examples to be presented shortly, the number of iterations vary from 1 to 2 (rarely 3) in every time step. If the Newton–Raphson method does not converge in a time step, we suggest to cut the time step inside the fractures through the multiple iterations, and the time step is kept intact in the matrix. There was not need to cut the fracture time step in our calculations. We used the iterative Pardiso_solver included in the Intel kernel library to solve the linear system of equations from Eq. (23). Next we discuss how to calculate the upstream value of $\bar{c}^{f,n}_{i,e}$ for multiple intersecting fractures.

Table 5
CPU time in seconds for different mesh refinements, at 1.0 PVI. Example 3.

Number of elements	400	900	1600-1	1600-2
CFE	6	–	38	221
FCFE	4	11	–	–

5.3. Upstream technique for multiple intersecting fractures

When there are only two intersecting fractures, the upstream value is simply deduced from the flux direction. For multiple intersecting fractures we use a generalization of the upstream for two intersecting fractures [1,26]. When n_t fractures intersect at a single point O, some of the fracture fluxes are in the upstream direction (we denote the number by an integer n_u) with respect to the intersection and the rest should be in the downstream direction in order to satisfy zero accumulation at the intersection:

$$\sum_{j=1}^{n_u}q^f_{k_j}+\sum_{j=n_u+1}^{n_t}q^f_{k_j}=\sum_{j=1}^{n_t}q^f_{k_j}=0 \tag{24}$$

The total mass balance of component i at the intersection point O is expressed by:

$$\sum_{j=1}^{n_u}c^f_{i,k}q^f_{k_j}=-c^f_{i,O}\sum_{j=n_u+1}^{n_t}q^f_{k_j} \tag{25}$$

Substituting Eq. (24) in Eq. (25) we obtain the upstream value at the intersection of n_t fractures as follows:

$$c^f_{i,O}=\frac{\sum_{j=1}^{n_u}c^f_{i,k}q_{k_j}}{\sum_{j=1}^{n_u}q_{k_j}} \tag{26}$$

Eq. (26) is a generalization of the upstream technique for two intersections. Verification is made by ($n_t = 2$) in Eqs. (24)–(26). Note that the set of Eqs. (24)–(26) are used for each component i in the mixture.

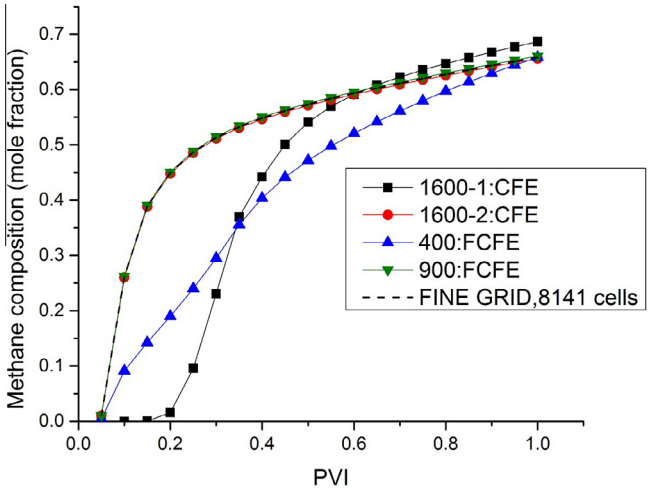

Fig. 11. Methane composition at the production well as a function of PVI. Example 3.

Table 6
Relevant properties of porous media of the fractured reservoir. Example 4a.

Matrix permeability [md]	1
Fracture permeability [md]	1.d6
Fracture thickness [mm]	0.1
Porosity [–]	0.2
Injection rate [PV/year]	0.5

6. Numerical examples

In the following we present four numerical examples with the number of species varying from 2 to 7 in structured grids to investigate the efficiency of the proposed approach. Extension to unstructured gridding will be presented in a future publication. In the first example the domain is unfractured to reconfirm that the higher-order algorithm is superior to the classical FD (FV) scheme; this efficiency has been demonstrated in [31,32]. In the other examples our FCFE algorithm is compared to the CFE approach. An Intel Core-i5 PC, 3 GHZ CPU, 4 GBRAM is used in all the runs.

6.1. Example 1: unfractured media

In the first example we consider a homogenous 2D horizontal domain of $50 \times 50\ m^2$ that is initially saturated with propane (C_3). A mixture of methane and ethane (C_1/C_2) is injected at the bottom left corner to displace C_3 to the opposite top right corner. The relevant data of this example are shown in Table 1. In Fig. 3 we show a comparison of the MFE-DG to MFE-FD in a 40×40 rectangular mesh at different PV injections. Results show the high numerical dispersion of the FD method compared to the higher-order model. Even with very refined meshes of 80×80 and 200×200 (results not shown) the FD result remains diffusive compared to the 40×40 MFE-DG solutions. For the same accuracy, the higher-order method is 2–3 orders of magnitude faster than the FD method.

6.2. Example 2: fractured media with two intersecting fractures

This example demonstrates the efficiency of our proposed model in fractured media. We consider two intersecting fractures in the $50 \times 50\ m^2$ horizontal domain (Fig. 4). Each fracture is 20 m long and the two fractures intersect at the center of the domain. A mixture of methane and ethane (C_1/C_2) is injected at one corner; production is from the opposite corner. Rock matrix data, fluid composition and injection rate are the same as in Example 1. Relevant data are provided in Table 2. In the CFE approach with a coarse mesh of 400 elements, the composition profile (Fig. 5a) shows that the matrix elements near the fractures are completely saturated with the injected gas. With a coarse mesh of 400 elements (Fig. 5b) the FCFE model gives accurate composition and the flow directions of the streamlines. Because the permeability in the fractures is 10^6 times higher than the matrix permeability, the fractures are the main flow channel to outlet. In the CFE approach the coarse mesh cannot provide similar composition profile to the FCFE model unless the mesh is refined near the fractures. Comparing the streamlines in Fig 5a and b one observes that at the fractures intersection, the CFE approach does not show a difference between the fracture network and the adja-

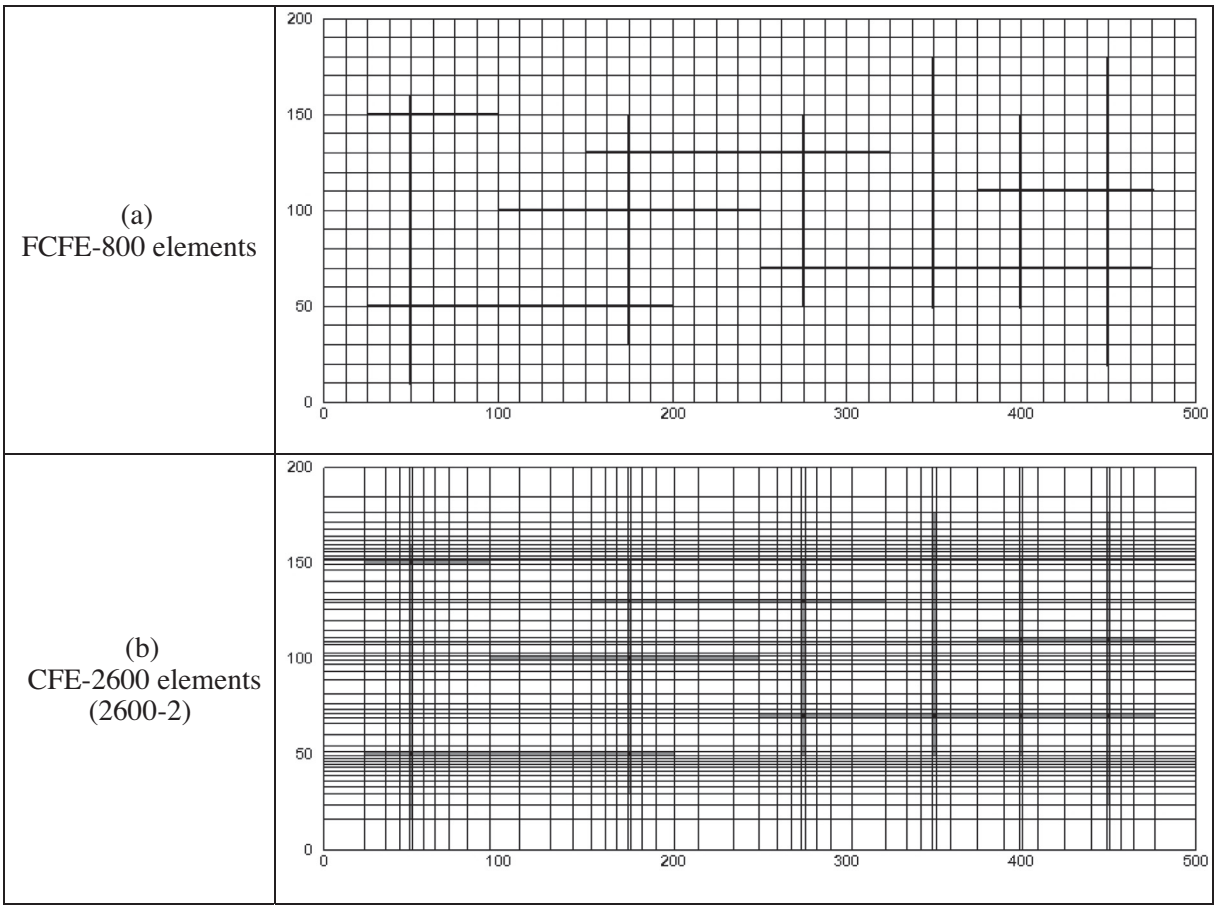

Fig. 12. Domain size of $500 \times 200\ m^2$ and mesh in the FCFE (a) and CFE (b) methods. Example 4 (distances in meters).

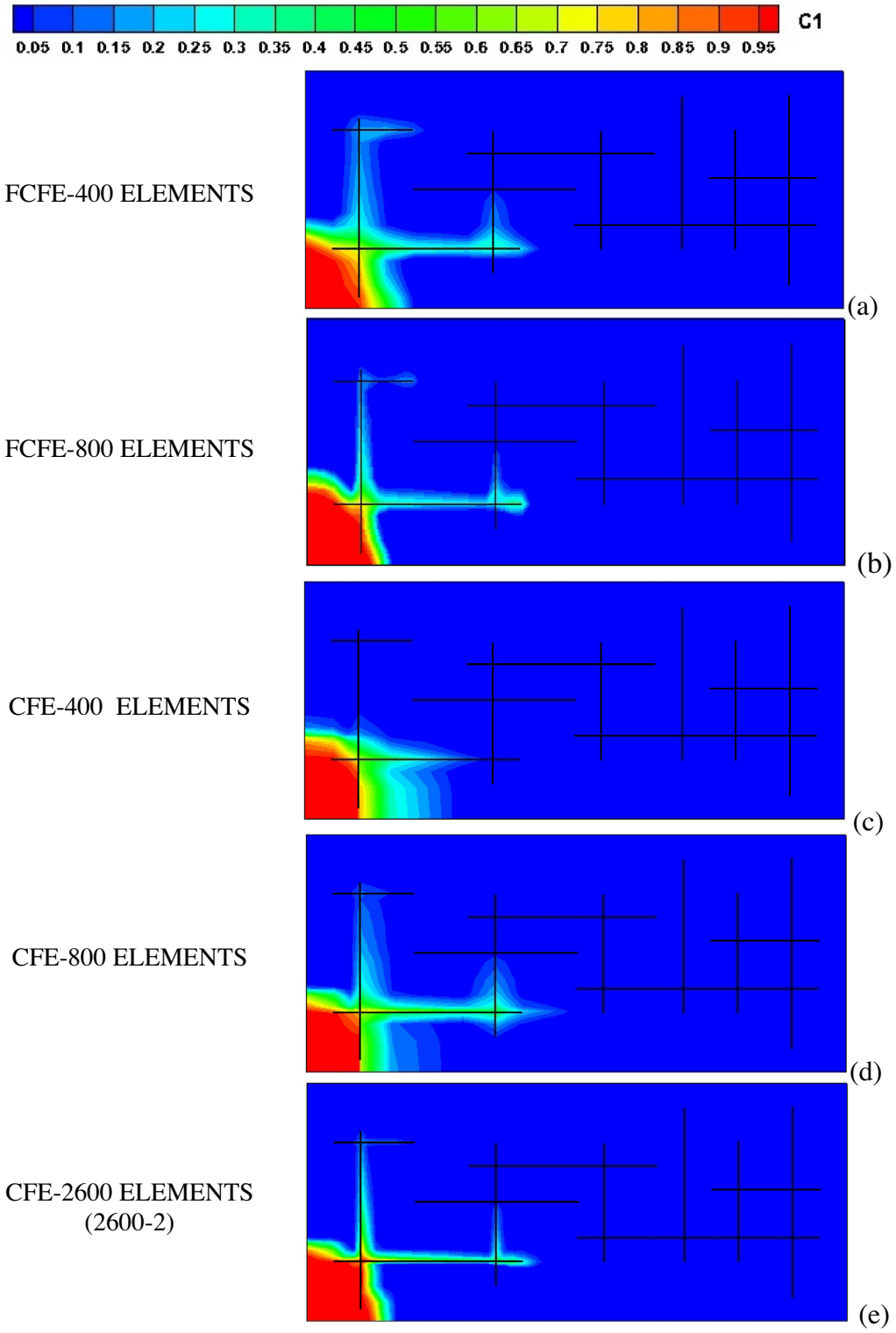

Fig. 13. Methane composition (mole fraction) profile at 0.05 PVI in the FCFE and CFE methods. Example 4a.

cent matrix elements. In the CFE approach one needs to refine the mesh to 3600 elements (Fig. 5c) to provide comparable results to 800 elements in the FCFE (Fig. 5d). In this simple fracture intersection, the FCFE model is more than 25 times faster than the CFE approach (see Table 3).

6.3. Example 3: sugar cube fracture configuration

In this example we consider an intensely fractured network. The domain size is $50 \times 50\,m^2$ (Fig. 6). The relevant data of the example are shown in Table 4. In the FCFE model two different

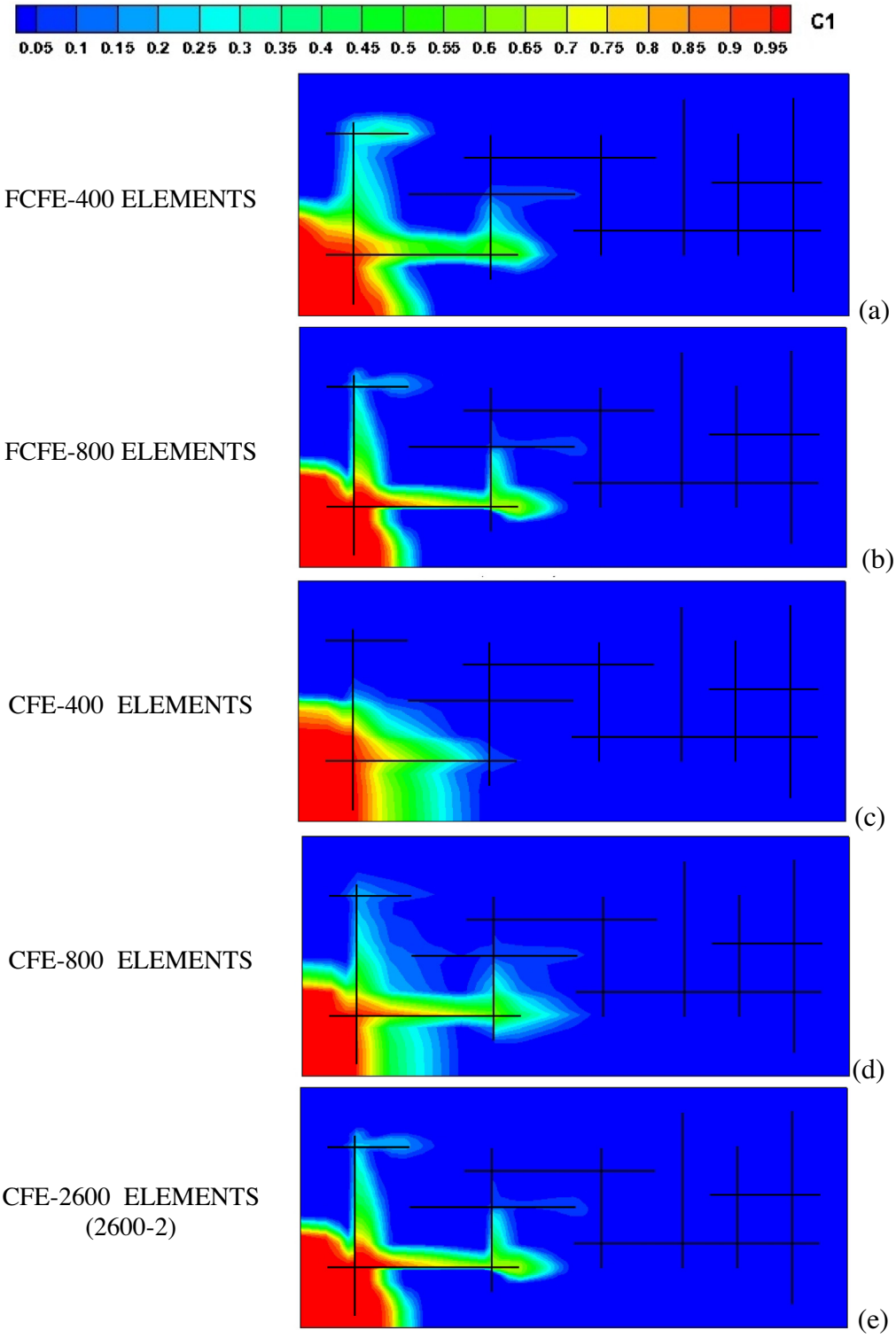

Fig. 14. Methane composition (mole fraction) profile at 0.1 PVI in the FCFE and CFE methods. Example 4a.

mesh refinements of 400 elements and 900 elements are used. In the CFE model we use 400 elements, and two types of 1600 elements designated by 1600-1 and 1600-2. In the grid 1600-1, the size of the matrix elements next to the fractures is set to 25 cm; the size of the matrix elements next to the fractures is set to 5 cm in the grid 1600-2. The two models are compared at 5%, 10%, 20%, 40% and 80% PVI. In the FCFE model, the composition profile results from the coarse mesh of 400 elements and the refined mesh of 900 elements (Figs. 7–10) are similar. The results are substantially different from those obtained with a more refined mesh in the CFE approach. Even in a refined mesh with 1600 elements (mesh 1600-1) the CFE model cannot provide comparable results to the coarse mesh of 400 elements in FCFE at PVI of 5% and 10% (Figs. 7 and 8). When the size of the matrix elements near

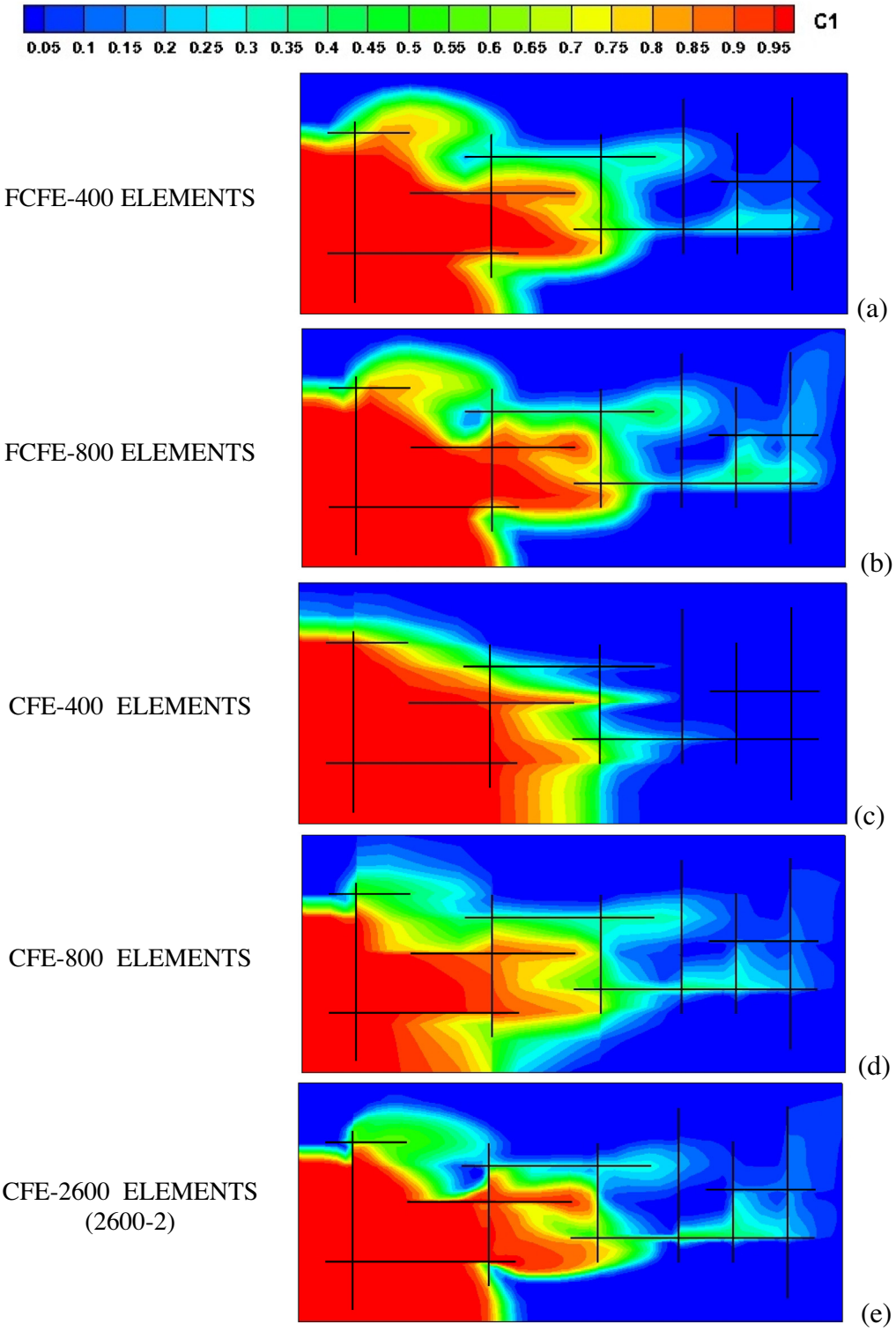

Fig. 15. Methane composition (mole fraction) profile at 0.4 PVI in the FCFE and CFE methods. Example 4a.

the fracture is reduced to 5 cm (mesh 1600-2), the CFE model starts to give comparable results to the 900 elements with the FCFE model. The CPU time of the FCFE model is 20 times less than the CFE for comparable results (Table 5). Fig. 11 shows methane composition at the production well for different mesh refinements in the two models as well as results from a refined mesh of 8142 elements. The refined mesh is used as a pseudo-analytical solution. There is substantial difference between the breakthrough time of CFE 1600-1 mesh and the fine mesh results.

6.4. Example 4a: fractured porous media with 2-component mixture

The computational domain in this example is $500 \times 200\ m^2$; it includes a set of distributed intersecting fractures. The relevant

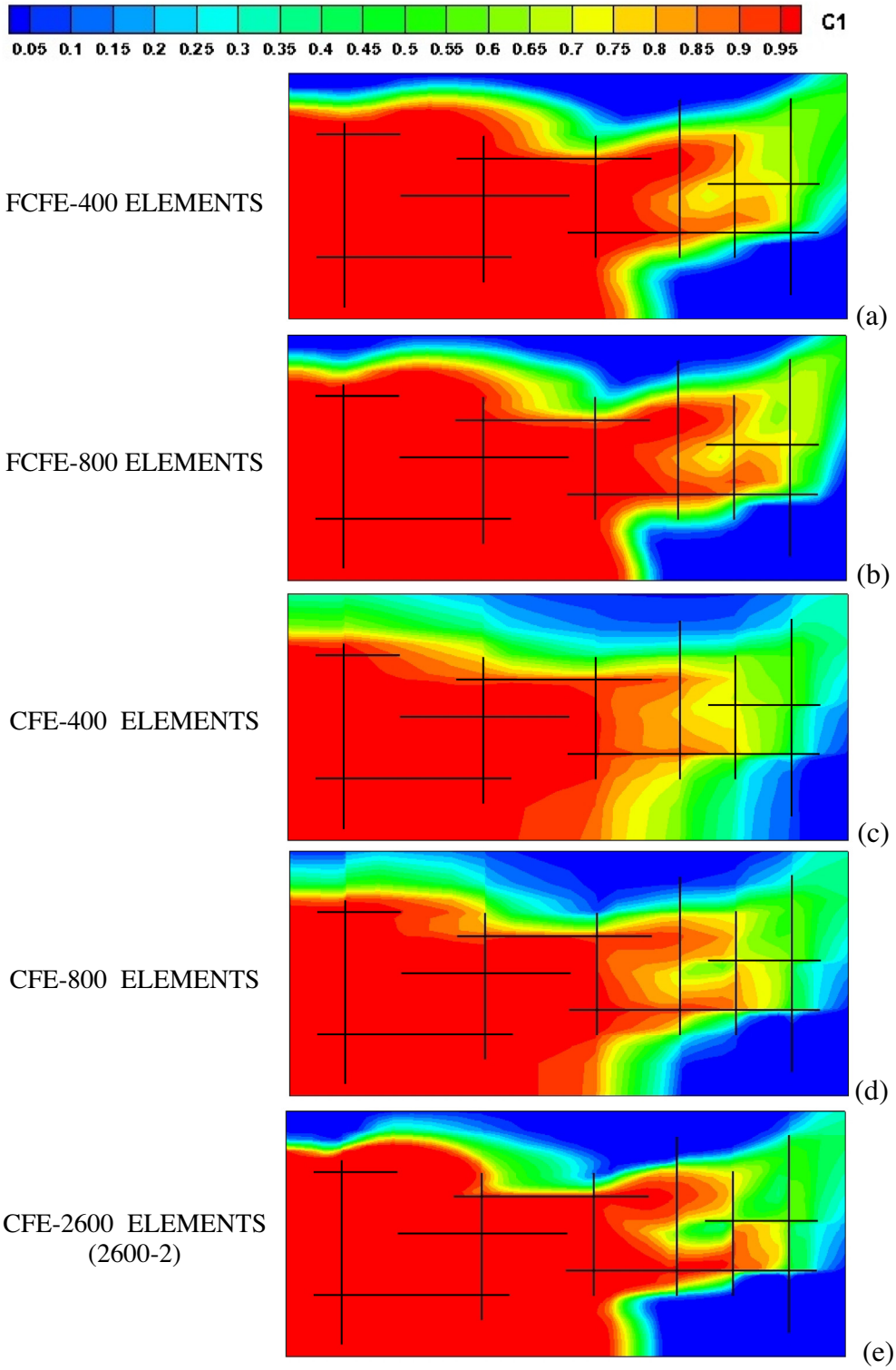

Fig. 16. Methane composition (mole fraction) profile at 0.8 PVI in the FCFE and CFE methods. Example 4a.

data of the example are shown in Table 6. Two mesh types are used in the FCFE model with 400 elements and 800 elements. In the CFE model we use four mesh refinements of 400, 800 and two types of 2600 elements that we denote by 2600-1 and 2600-2. In the 2600-1 grid, the size of the matrix elements near the fractures varies from 1 to 2 m. In 2600-2 the size of the matrix elements near the fractures varies from 0.3 to 0.4 m. The mesh of 800 elements with the FCFE model and the 2600-2 with the CFE model are shown in Fig. 12. The injection rate is set to 0.5 PV/year. The results for both models are compared at PV injections of 5%, 10%, 40%, 80% and 120%. In Figs. 13–17 we show the results of the 400 and 800 elements of FCFE model and the

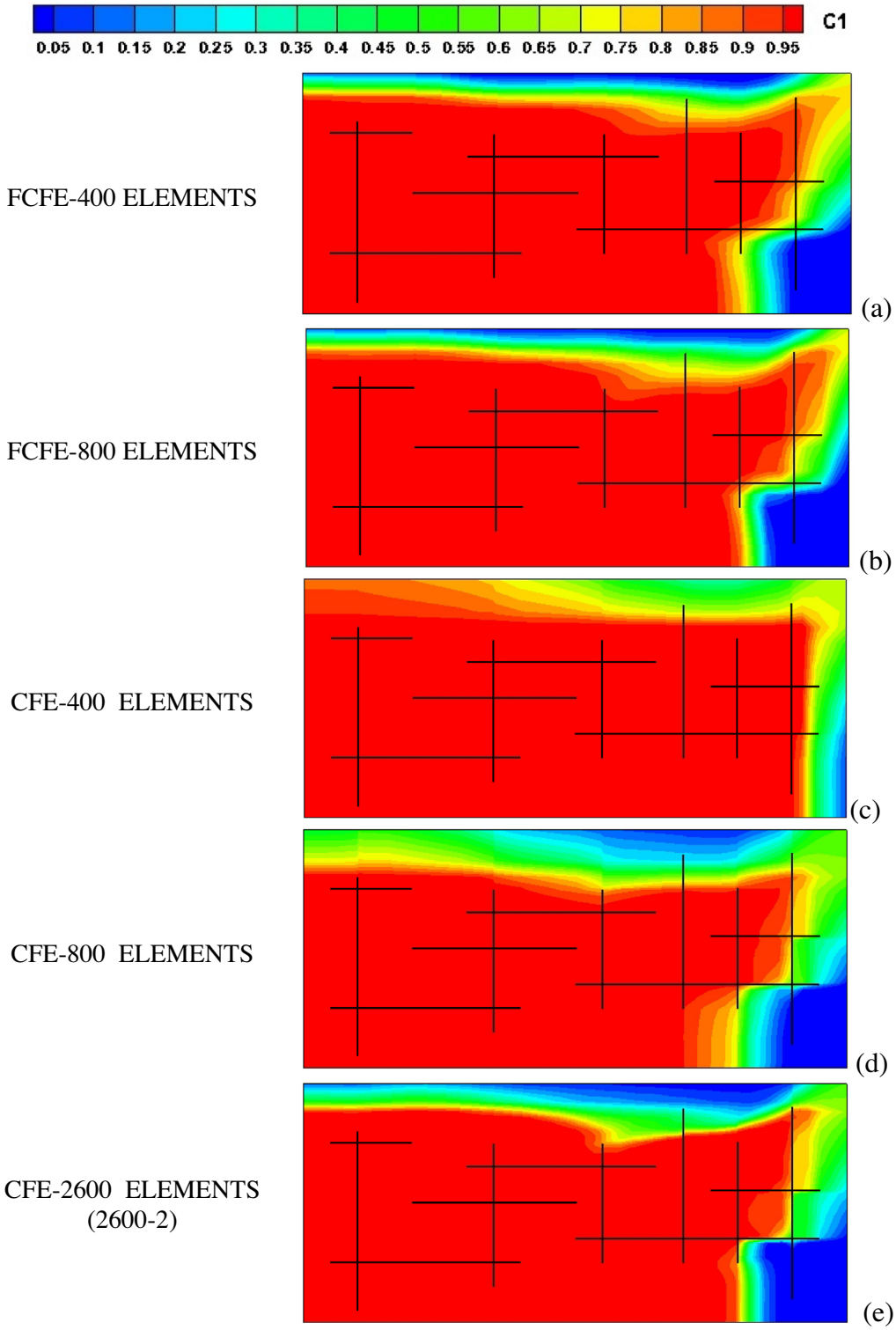

Fig. 17. Methane composition (mole fraction) profile at 1.2 PVI in the FCFE and CFE methods. Example 4a.

results of 400, 800 and 2600-2 of the CFE model. The CFE model does not produce accurate results with 400 elements (Figs 13–17). The 800 elements in the CFE model start to give comparable results to the 400 elements in the FCFE model; however, even with 800 elements the CFE results look more diffusive when compared to the 400-FCFE elements. For comparable results to the 800 elements in FCFE one needs to refine the mesh in the CFE model to 2600 elements and reduce the size of the matrix elements near the fractures. In the 2600-2 mesh of the CFE model, the size of the matrix elements near the fractures are reduced to 0.3 m in order to obtain comparable results to the 800 elements of the FCFE model (Figs. 13–17).

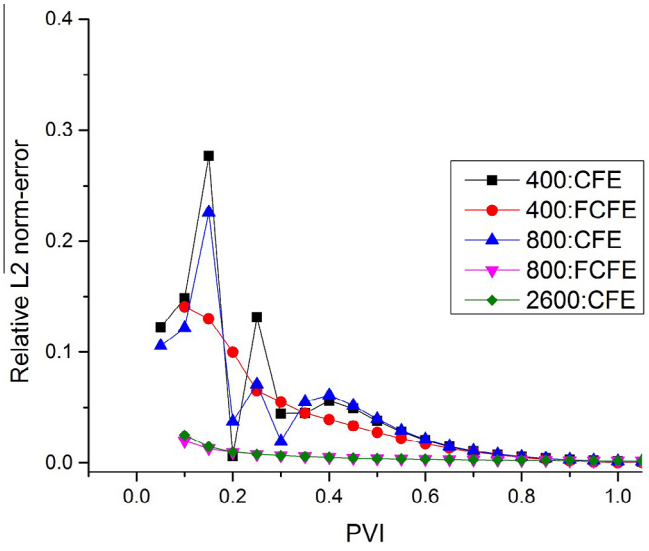

Fig. 18. Relative L2 norm error for different griddings. Example 4a.

Table 7
CPU time in seconds for different mesh refinements at 1.5 PVI. Example 4a.

Number of elements	400	800	2600-1	2600-2
CFE	8	124	1747	7260
FCFE	6	55	–	–

A relative second order L^2 norm error is used to compare the CFE and FCFE models to a fine grid with 8241 elements. The relative error is plotted as a function of PVI (Fig. 18) for a point near the injection well to compare methane composition to the fine-grid results. The over and under shoots of the 400-CFE and 800-CFE plots is due to the fact that at low PVI and with large matrix elements near the fractures the pressure and compositions are not accurate compared to the refined (pseudo-analytical) values. At high PVI the domain starts to be saturated by the injected methane and therefore the relative error goes to zero. The plots of the 800-FCFE and 2600-CFE show that the error with these gridding is very low (2%) even at low PVI.

The FCFE model is about 130 times faster than the CFE approach (Table 7) for the above gridding.

6.5. Example 4b: fractured porous media with 7-component mixture

This example is similar to example 4a except that the mixture contains 7 components. Methane is injected into the domain that is saturated with a 6-component mixture. The relevant data are given in (Table 8). The high number of components requires higher cost for the matrix inversions in the NR method. As a result, higher CPU time is required in the FCFE approach compared to the two-component example. In the 7 components, convergence is reached in 91 s whereas 55 s are required in the 2-component mixture with the same mesh (800-FCFE). The impact of the number of components on the CPU time in the CFE approach is less than in the FCFE approach. As a result, 8840 s are needed in the 2600-2 mesh compared to 7260 s with the same mesh in the two-component mixture. Superiority of the FCFE in the multicomponent mixture is preserved although to a lesser degree over the CFE approach. The FCFE is two orders of magnitude faster than the CFE in the multicomponent example (Table 9).

Table 9
CPU time in seconds for different mesh refinements at 1.5 PVI. Example 4b.

Number of elements	400	800	2600-1	2600-2
CFE	10	153	2185	8840
FCFE	9	91	–	–

In addition to the above examples, we have also made a run with the domain in Example 4 saturated with normal dodecane. Propane is then injected at the same rate as in Example 4. The temperature and pressure are fixed at 313 K and 100 bar, respectively. The viscosity of dodecane is 15 times higher than propane at the selected conditions. Results and performance of the CFE and FCFE approaches are comparable to Example 4a.

7. Conclusions

We have introduced an efficient numerical model based on the concept of fracture cross flow equilibrium (FCFE) in the higher-order MFE-DG algorithm to simulate multicomponent compressible flow in fractured media. The features of the proposed model are:

- A constant pressure is assumed along the fracture width. As a result one can have large matrix grid-cells next to the fractures.
- The large matrix grid-cells near the fractures allow large time steps in the matrix which reduces the CPU cost.
- We use an implicit scheme for species transport in the fracture network. The implicit scheme palliates the restriction on the time step size from the CFL condition.

Compared to the CFE approach, the proposed model is found to be 20–130 times faster in the 2-D examples we have selected. We expect a larger difference between the FCFE and CFE methods in 3-D and in more complex domains because the very small size of fracture intersections compared to other grid fracture elements. In 3-D the severe CFL constraint for small fracture intersection elements will make the FCFE model much more efficient. Implementation of the proposed approach to two-and three-phase flows, with gravity in 2-D and 3-D, and with adsorption effect are being currently investigated.

Table 8
Relevant data (T_c, P_c and V_c are respectively the critical temperature, critical pressure and critical mass volume and M_w is the molar weight). Example 4b.

Component	Tc (K)	Pc (bar)	Vc (m^3/kg)	Acentric factor	M_w (g/mole)	Shift Parameter	Injected gas (mole fraction)	Initial fluid (mole fraction)
CH_4	190.56	45.99	0.00614614	0.011	16.04	−0.154	1.0	0.0
C_2H_6	305.32	48.72	0.00483881	0.099	30.07	−0.1002	0.0	0.24
C_3H_8	369.83	42.48	0.00453554	0.153	44.10	−0.08501	0.0	0.13
C_4H_{10}	407.80	36.04	0.00445607	0.183	58.12	−0.07935	0.0	0.18
C_5H_{12}	460.40	33.80	0.00424118	0.227	72.15	−0.0435	0.0	0.11
CO_2	304.1	3.8	0.0021	0.24	44	0.06	0.0	0.19
N_2	126.2	33.9	0.0032	0.04	28	−0.289	0.0	0.14

Acknowledgement

This work was supported by the member companies of the Reservoir Engineering Research Institute (RERI). The support is gratefully acknowledged.

Appendix A

The single-phase compressibility can be calculated from [see e.g. 53].

$$C_t = \frac{V^{EOS}}{V}\left[\frac{1}{P} - \frac{1}{Z}\left(\frac{\partial Z}{\partial P}\right)_{T,n}\right] \tag{A.1}$$

V and V^{EOS} are the molar volumes with and without the volume shifts, respectively. The partial molar volume of component i is given by [see e.g. 53]:

$$\bar{V}_i = \frac{NRT}{P}\left(\frac{\partial Z}{\partial n_i}\right)_{T,P,n\neq i} + V^{EOS} + s_i \tag{A.2}$$

N is the total number of moles, $V^{EOS} = ZRT/P$, and s_i is the volume shift of component i.

Appendix B

For completeness we present briefly the MFE discretization; further details can be found in [1,37]. In the MFE, the velocity over each cell is expressed with respect to the fluxes across the edges. The Raviart–Thomas basis functions on a rectangular gird element K that has a width d_x and a height d_y and a surface area $|K| = d_x d_y$ are given by:

$$w_{K,E_1} = \frac{1}{d_x d_y}\begin{pmatrix} x + \frac{d_x}{2} \\ 0 \end{pmatrix} \tag{B.1}$$

$$w_{K,E_2} = \frac{1}{d_x d_y}\begin{pmatrix} x - \frac{d_x}{2} \\ 0 \end{pmatrix} \tag{B.2}$$

$$w_{K,E_3} = \frac{1}{d_x d_y}\begin{pmatrix} 0 \\ y - \frac{d_y}{2} \end{pmatrix} \tag{B.3}$$

$$w_{K,E_4} = \frac{1}{d_x d_y}\begin{pmatrix} 0 \\ y - \frac{d_y}{2} \end{pmatrix} \tag{B.4}$$

where E_i denotes the edge i of the element K as follows: 1 = *Right*, 2 = *Left*, 3 = *Top*, 4 = *Bottom*.

The above vector functions are linearly independent and they satisfy the following properties:

$$\nabla \cdot w_{K,E} = \frac{1}{|K|} \tag{B.5}$$

$$w_{K,E} \cdot n_{E'} = \begin{cases} \frac{1}{|E|} & \text{if } E = E' \\ 0 & \text{else} \end{cases} \tag{B.6}$$

The velocity field can be written with respect to the basis functions $w_{K,E}$ as follows

$$\boldsymbol{v} = \sum_E q_{K,E} \boldsymbol{W}_{K,E} \tag{B.7}$$

where $q_{K,E}$ denotes the flux across the edge E of the element K.

Inverting the mobility tensor $\mathbf{K}$ ($\mathbf{K} = \boldsymbol{k}/\mu$), Darcy's equation becomes

$$\mathbf{K}^{-1}\boldsymbol{v} = -(\nabla p - \rho g) \tag{B.8}$$

Table B1
Dimensions and expressions of the matrices in Eq. (12).

Matrix	Dimensions	Expression
$R^{T,m,m}$	$N_K^m \times N_E^m$	$R^{T,m,m}_{K,E} = \alpha^m_{K,E}$
$R^{T,m,f}$	$N_K^m \times N_k^f$	$R^{T,m,f}_{K,E} = \alpha^m_{K,E}$
$M^{m,m}$	$N_E^m \times N_E^m$	$M^{m,m}_{E,E'} = \sum_{E'\partial K}\beta^m_{K,E,E'}$
$M^{m,f}$	$N_k^f \times N_k^f$	$M^{m,f}_{E,E'} = \sum_{E'\partial K}\beta^m_{K,E,E'}$
$M^{f,f}$	$N_e^f \times N_e^f$	$M^{f,f}_{E,E'} = \sum_{E'\partial K}\beta^m_{K,E,E'}$

where $\boldsymbol{k}$ is the absolute permeability and μ the dynamic viscosity.

By multiplying Eq. (B.7) by the test function $w_{K,E}$ and integrating we get:

$$\int_K w_{K,E}\mathbf{K}^{-1}\boldsymbol{v} = -\int_K w_{K,E}(\nabla p - \rho g) \tag{B.9}$$

Using Eqs. (B.5)–(B.7) in (B.9) yield:

$$\sum_{E'} q_{K,E'}\int_K W_{K,E}\mathbf{K}^{-1}w_{K,E'} = P_K - Tp_{K,E'} \tag{B.10}$$

where P_K is the cell average pressure and $Tp_{K,E'}$ is the edge average pressure. Inverting the integral term at the left hand side we get:

$$q_{K,E} = \alpha_{K,E}P_K - \sum_{E'}\beta_{K,E,E'}\,Tp_{K,E'} \tag{B.11}$$

where

$$\alpha_{K,E} = \sum_{E'}\beta_{K,E,E'}$$

$$\beta_{K,E,E'} = (B_K^{-1})_{E,E'}; \quad B_{K,E,E'} = \int_K W_{K,E}\mathbf{K}^{-1}W_{K,E'}$$

We define the following notation in the matrix and fractures:
N_K^m: Number of grid-cells in the matrix.
N_E^m: Number of non-fracture interfaces in mesh.
N_k^f: Number of grid-cells in the fracture network.
N_e^f: Number of fracture–fracture interfaces in the fracture network.
The matrices in Eq. (12) are defined in the Table B1.

References

[1] Hoteit H, Firoozabadi A. An efficient model for incompressible two-phase flow in fractured media. Adv Water Resour 2008;31:891–905. http://dx.doi.org/10.1016/j.advwatres.2008.02.004.
[2] Karimi-Fard M, Durlofsky LJ, Aziz K. An efficient discrete-fracture model applicable for general purpose reservoir simulators. SPE J 2004;9:227–36. http://dx.doi.org/10.2118/88812-PA.
[3] Kim JG, Deo MD. Finite-element, discrete-fracture model for multiphase flow in porous media. AIChE J 2000;46(6):1120–30. http://dx.doi.org/10.1002/aic.690460604.
[4] Matthäi SK, Mezentsev A, Belayneh M. Finite element node-centered finite-volume experiments with fractured rock represented by unstructured hybrid element meshes. SPE Reservoir Eval Eng 2007;10(6):740–56. http://dx.doi.org/10.2118/93341-PA.
[5] Matthäi SK, Geiger S, Roberts SG, Paluszny A, Belayneh M, Burri A, Mezentsez A, Lu H, Coumou D, Driesner T, Heinrich CA. Numerical simulation of multiphase fluid flow in structurally complex reservoirs. Special Publications, Geological Society, London Geological Society, London 2007;292: pp. 405–429. http://dx.doi.org/10.1144/SP292.22.
[6] Reichenberger V, Jakobs H, Bastian P, Helmig R. A mixed-dimensional finite volume method for multiphase flow in fractured porous media. Adv Water Resour 2006;29:1030–6. http://dx.doi.org/10.1016/j.advwatres.2005.09.001.
[7] Schmid KS, Geiger S, Sorbie KS. Higher order FE–FV method on unstructured grids for transport and two-phase flow with variable viscosity in heterogeneous porous media. J Comput Phys 2013(241):P416–44. http://dx.doi.org/10.1016/j.jcp.2012.12.017.
[8] Geiger S, Matthäi S, Niessner J, Helmig R, et al. Black-oil simulations for three-component, three-phase flow in fractured porous media. SPE J 2009;14(2):338–54. http://dx.doi.org/10.2118/107485-PA.

[9] Sandve TH, Berre I, Nordbotten JM. An efficient multi-point flux approximation method for discrete fracture-matrix simulations. J Comput Phys 2012(231):3784–800. http://dx.doi.org/10.1016/j.jcp.2012.01.023.

[10] Nick HM, Matthäi SK. Comparison of three FE-FV numerical schemes for single- and two-phase flow simulation of fractured porous media. Transp Porous Media 2011;90:421–44. http://dx.doi.org/10.1007/s11242-011-9793-y.

[11] Barenblatt G, Zheltov Y, Kochina I. Basic concepts in the theory of seepage of homogeneous fluids in fissurized rocks. J Appl Math Mech 1960;24(5):1286–303. http://dx.doi.org/10.1016/0021-8928(60)90107-6.

[12] Warren J, Root P. The behavior of naturally fractured reservoirs. SPE J 1963:245–55. http://dx.doi.org/10.2118/426-PA.

[13] Gilman JR, Kazemi H. Improvement in simulation of naturally fractured reservoirs. SPE J 1983;23:695–707. http://dx.doi.org/10.2118/10511-PA.

[14] Thomas L, Dixon T, Pierson R. Fractured reservoir simulation. SPE J 1983:42–54. http://dx.doi.org/10.2118/9305-PA.

[15] Kazemi H, Gilman J. Pressure transient analysis of naturally fractured reservoirs with uniform fracture distribution. SPE J December 1969:451–62. http://dx.doi.org/10.2118/2156-A.

[16] Kazemi H, Gilman J. Analytical and numerical solution of oil recovery from fractured reservoirs with empirical transfer functions. SPE J May 1992:219–27. http://dx.doi.org/10.2118/19849-PA.

[17] Kazemi H, Merrill L. Numerical simulation of water imbibition in fractured cores. SPE J June 1979:175–82. http://dx.doi.org/10.2118/6895-PA.

[18] Quandalle P, Sabathier JC. Typical features of a multipurpose reservoir simulator. SPE Res Eng 1989;4(4):475–80. http://dx.doi.org/10.2118/16007-PA.

[19] Haggerty R, Gorelick SM. Multiple-rate mass transfer for modelling diffusion and surface reactions in media with pore-scale heterogeneity. Water Resour Res 1995;31(10):2383–400. http://dx.doi.org/10.1029/95WR10583.

[20] Di Donato G, Lu HY, Taasoli Z, et al. Multi-rate-transfer dual-porosity modeling of gravity drainage and imbibition. SPE J 2007;12(1):77–88. http://dx.doi.org/10.2118/93144-MS.

[21] Geiger S, Dentz M, Neuweiler I. A novel multirate dual-porosity model for improved simulation of fractured and multiporosity reservoirs. SPE J August 2013:670–84. http://dx.doi.org/10.2118/148130-PA.

[22] Unsal E, Stephan K, Matthäi SK, Martin JB. Simulation of multiphase flow in fractured reservoirs using a fracture-only model with transfer functions. Comput Geosci 2010;14:527–38. http://dx.doi.org/10.1007/s10596-009-9168-4.

[23] Gouze P, Borgne L, Leprovost R. Non-Fickian dispersion in porous media: 1.Multiscale measurements using single well injection withdrawal tracer tests at the ses sitjoles/aliance test site (Spain). Water Resour Res 2008;44. http://dx.doi.org/10.1029/2007WR006278.

[24] Moortgat J, Firoozabadi A. Fickian diffusion in discrete-fractured media from chemical potential gradients and comparison to experiment. Energy Fuels 2013;27:5793–805. http://dx.doi.org/10.1021/ef401141q.

[25] Bastian P, Helmig R, Jakobs H, Reichenberger V. Numerical simulation of multiphase flow in fractured porous media. In: Numerical treatment of multiphase flows in porous media. In: Chen, Ewing, Shi, editors. Lecture notes in physics, vol. 552. Springer-Verlag; 2000. p. 1–18.

[26] Bogdanov I, Mourzenko V, Thovert J, Adler P. Two-phase flow through fractured porous media. Phys Rev E 2003;68(2):1–24. http://dx.doi.org/10.1103/PhysRevE.68.026703.

[27] Geiger S, Roberts S, Matthäi S, Zoppou C, Burri A. Combining finite element and finite volume methods for efficient multiphase flow simulations in highly heterogeneous and structurally complex geologic media. GeoFluids 2004;4(4):284–99. http://dx.doi.org/10.1111/j.1468-8123.2004.00093.x.

[28] Noorishad J, Mehran M. An upstream finite element method for solution of transient transport equation in fractured porous media. Water Resour Res 1982;18(3):588–96. http://dx.doi.org/10.1029/WR018i003p00588.

[29] Granet S, Fabrie P, Lemmonier P, Quintard M. A single phase flow simulation of fractured reservoir using a discrete representation of fractures. In: Proceedings of the 6th European conference on the mathematics of oil recovery (ECMOR VI), September 8–11, Peebles, Scotland, UK; 1998.

[30] Hoteit H, Firoozabadi A. Multicomponent fluid flow by discontinuous Galerkin and mixed methods in unfractured and fractured media. Water Resour Res 2005;41(11):W11412. http://dx.doi.org/10.1029/2005WR004339.2005.

[31] Hoteit H, Firoozabadi A. Numerical modeling of diffusion in fractured media for gas injection and recycling schemes. In: Annual technical conference and exhibition, 4–27 September, San Antonio, TX; 2006. No. SPE103292. http://dx.doi.org/10.2118/103292-MS.

[32] Durlofsky L. Accuracy of mixed and control volume finite element approximations to Darcy velocity and related quantities. Water Resour Res 1994;30(4):965–73. http://dx.doi.org/10.1029/94WR00061.

[33] Mosé R, Siegel P, Ackerer P, Chavent G. Application of the mixed hybrid finite element approximation in a ground water flow model: luxury or necessity. Water Resour Res 1994(11):3001–12. http://dx.doi.org/10.1029/94WR01786.

[34] Darlow B, Ewing R, Wheeler M. Mixed finite element method for miscible displacement problems in porous media. SPE J 1984;24:391–8. http://dx.doi.org/10.2118/10501-PA.

[35] Hoteit H, Firoozabadi A. Compositional modeling by the combined discontinuous Galerkin and mixed methods. SPE J 2006;11(1):19–34. http://dx.doi.org/10.2118/90276-MS.

[36] Hoteit H, Firoozabadi A. Compositional modeling of discrete-fractured media without transfer functions by the discontinuous Galerkin and mixed methods. SPE J 2006;11(3):341–52. http://dx.doi.org/10.2118/90277-PA.

[37] Hoteit H, Firoozabadi A. Numerical modeling of two-phase flow in heterogenous permeable media with different capillarity pressures. Adv Water Resour 2008;31:56–73. http://dx.doi.org/10.1016/j.advwatres.2007.06.006.

[38] Cockburn B, Shu C. TVB Runge–Kutta local projection discontinuous Galerkin finite element method for conservative laws II: general frame-work. Math Comput 1989;52:411–35.

[39] Cockburn B, Shu C. The Runge–Kutta discontinuous Galerkin method for conservative laws V: multidimensional systems. J Comput Phys 1998;141:199–224. http://dx.doi.org/10.1006/jcph.1998.5892.

[40] Chavent G, Jaffré J, editors. Mathematical models and finite elements for reservoir simulation. Studies in mathematics and its applications. North-Holland: Elsevier; 1986.

[41] Hoteit H, Ackerer P, Mosé R. Nuclear waste disposal simulations: couplex test cases. Comput Geosci 2004;8(2):99–124. http://dx.doi.org/10.1023/B:COMG.0000035074.37722.71.

[42] Younes A, Fahs M, Ahmed S. Solving density driven flow problems with efficient spatial discretizations and higher-order time integration methods. Adv Water Resour 2009;32:340–52. http://dx.doi.org/10.1016/j.advwatres.2008.11.003.

[43] Siegel P, Mosé R, Ackerer P, Jaffre J. Solution of the advection-diffusion equation using a combination of discontinuous and mixed finite elements. Int. J Numer Methods Fluids 1997;24(6):595–613. http://dx.doi.org/10.1002/(SICI)1097-0363(19970330)24:6<595::AID-FLD512>3.0.CO;2-I.

[44] Monteagudo J, Firoozabadi A. Comparison of fully-implicit and IMPES formulations for simulation of water injection in fractured and unfractured media. Int J Numer Methods Eng 2006;69(4):698–728. http://dx.doi.org/10.1002/nme.1783.

[45] Kim J, Deo M. Comparison of the performance of a discrete fracture multiphase model with those using conventional methods. In: Reservoir simulation symposium, 14–17 February, Houston, TX; 1999. No. SPE51928. http://dx.doi.org/10.2118/51928-MS.

[46] Bastian P, Helmig R. Efficient fully-coupled solution techniques for two-phase flow in porous media. parallel multigrid solution and large scale computations. Adv Water Resour 1999;23:199–216. http://dx.doi.org/10.1016/S0309-1708(99)00014-7.

[47] Karimi-Fard M, Firoozabadi A. Numerical simulation of water injection in 2D fractured media using discrete-fracture model. SPEREE J 2003;4(March):117–26. http://dx.doi.org/10.2118/71615-MS.

[48] Moortgat J, Firoozabadi A. Higher-order compositional modeling with Fickian diffusion in unstructured and anisotropic media. Adv Water Resour 2010;33:951–68. http://dx.doi.org/10.1016/j.advwatres.2010.04.012.

[49] Moortgat J, Sun S, Firoozabadi A. Compositional modeling of three phase flow with gravity using higher order finite element methods. Water Resour Res 2011;47:W05511. http://dx.doi.org/10.1029/2010WR009801.

[50] Moortgat J, Li Z, Firoozabadi A. Three-phase compositional modeling of CO_2 injection by higher-order finite element methods with CPA equation of state for aqueous phase. Water Resour Res 2012;48:W12511. http://dx.doi.org/10.1029/2011WR011736.

[51] Moortgat J, Firoozabadi A. Higher-order compositional modeling of three-phase flow in 3D fractured porous media based on cross-flow equilibrium. J Comput Phys 2013;250:425–45. http://dx.doi.org/10.1016/j.jcp.2013.05.009.

[52] Peng DY, Robinson DB. A new two-constant equation of state. Ind Eng Chem Fundam 1976;15:59–64. http://dx.doi.org/10.1021/i160057a011.

[53] Firoozabadi A. Thermodynamics of hydrocarbon reservoirs. USA: McGraw-Hill Professional; 1999.

[54] Acs G, Doleschall S, Farkas E. General purpose compositional model. SPE J 1985;25(4):543–53. http://dx.doi.org/10.2118/10515-PA.

[55] Watts JW. A compositional formulation of the pressure and saturation equations. SPE Reservoir Eng 1986;1(3):243–52. http://dx.doi.org/10.2118/12244-PA.